Revisiting Ag addition in 7xxx aluminum alloys: Insights into its impact on the microstructure and properties of an Al-Zn-Mg-Cu-Zr alloy with a Zn/Mg ratio of 4

Chijioke Kenneth Akuata [a], Lisa T. Belkacemi [b,c], Daniela Zander [a,d,*]

[a] Chair of Corrosion and Corrosion Protection, Foundry Institute, Division of Materials Science and Engineering, RWTH Aachen University, Intzestraße 5, 52072 Aachen, Germany
[b] Leibniz-Institute for Materials Engineering – IWT, Badgasteiner Straße 3, 28359 Bremen, Germany
[c] MAPEX Center for Materials and Processes, University of Bremen, Bibliothekstraße 1, 28359 Bremen, Germany
[d] Deutsches Zentrum für Luft- und Raumfahrt, German Aerospace Center, Institute of Materials Physics in Space, Linder Höhe, 51147 Cologne, Germany

ABSTRACT

In this study, the influence of minor Ag addition on the microstructure, mechanical and corrosion properties of an Al-Zn-Mg-Cu-Zr (7449) alloy with Zn/Mg ratio of 4 was systematically investigated using various materials characterization techniques, Slow Strain Rate Test (SSRT), Potentiodynamic Polarization (PDP) and Intergranular Corrosion (IGC) measurements. Microstructure characterization by Scanning Electron Microscopy (SEM) and Differential Scanning Calorimetry (DSC) showed that Ag partitioning in the eutectic $Mg(Zn,Cu,Al)_2$ phase occurs resulting in an increase in its solvus line. After processing to the T4 condition, Ag was partially in solid solution with the excess forming an Ag-rich AlAgZnMgCu phase. Scanning-Transmission Electron Microscopy (STEM) showed evidence of quench-induced η-$Mg(Zn,Cu,Al)_2$ precipitates at the grain boundaries (GBs) in the T4 condition with ~3 at.% Ag in the Ag-modified alloy. STEM and Atom Probe Tomography (APT) confirmed that ~1 at. % Ag was present in both the matrix and GB precipitates in the Ag-modified alloy after T76 aging. Furthermore, the frequently reported decrease in the PFZ width with Ag addition was not observed after T76 aging, with both alloys having a similar PFZ width. Despite higher hardness/strength in the T4 condition with Ag addition, no enhanced age hardening response and alteration of the precipitation kinetics was observed during artificial aging at 121 °C. In fact, Ag addition in a 7xxx alloy with Zn/Mg ratio of 4 was found to be detrimental to mechanical properties, stress corrosion cracking, pitting and IGC resistance after T76 aging, which is attributed to the presence of the Ag-rich AlAgZnMgCu phase.

1. Introduction

For decades, high-strength 7xxx series aluminum alloys have proven to be indispensable for structural design in the aviation/aerospace industry, mainly due to their low cost, high specific strength, high damage tolerance and moderate corrosion resistance properties [1–3]. However, the growing need for cost optimization and particularly weight reductions to minimize fuel consumption and reduce CO_2 and NO_X emissions in the aforementioned industry has led to the promotion of structural concepts focusing on monolithic design. This design approach requires alloys with superior strength, improved through-thickness properties and high damage tolerance. This resulted in the

development of new, advanced 7xxx alloys and the optimization of the processing route [4]. These new generation 7xxx alloys were developed mainly by increasing the Zn/Mg ratio up to 5, lowering the Cu content and impurity levels (Fe, Si) to suppress the formation of coarse intermetallic particles (IMPs) and minimize dynamic recrystallization by particle stimulated nucleation (PSN) [5]. The improved strength properties of these alloys have, however, been to the detriment of their resistance to hydrogen environmentally assisted cracking (HEAC) [6–10].

In the last two decades, attention has shifted to Ag addition in 7xxx alloys. First studied in 1960 [11], trace amount of Ag is reported to accelerate the precipitation kinetics in both Cu-free and Cu-containing

7xxx alloys due to its strong attractive interaction with vacancy and solute atoms of Zn and Mg [12–22]. Vacancy diffusion to the grain boundaries (GBs) is believed to be hindered in the presence of Ag, ensuring enhanced nucleation and dispersion of Ag-vacancy and Ag-solute co-clusters which act as precursors for the formation of strengthening phases, resulting in increased hardening. The generally accepted precipitation sequence from supersaturated solid solution (SSSS) in 7xxx alloys is [23–25] $SSSS \rightarrow Guinier - Preston\ (GP)\ zones \rightarrow \eta' \rightarrow \eta - Mg(Zn, Cu, Al)_2$, with metastable GP zones and η' being responsible for enhanced strengthening, particularly after peak aging. However, depending on the alloy chemistry (Zn/Mg) and the aging temperature, the hardening polyhedral T $-Mg_{32}(Al,Zn,Cu)_{49}$ phase may form [18,26]. Previous investigations by Auld et al. [27], Maloney et al. [21] and Wang et al. [18], proposed that Ag addition enhanced the formation of T-type clusters/phase in Al-Cu-Mg, Al-Zn-Mg and Al-Zn-Mg-Cu alloy, respectively, which contributed to the enhanced strengthening in these alloys after artificial aging. But, contrary to these results, Hunsicker et al. [28] in a study on Al-Zn-Mg-Cu 7075 alloy observed no increase in strength with 0.3–0.4 wt% Ag addition after isothermal and two-step aging treatments. In fact, lower strength with minor Ag addition has been reported in previous investigations on 7075 [15] and 7085 alloys [29].

A decrease in the ubiquitous precipitate free zone (PFZ) width at the GB region after artificial aging is another crucial role of Ag in 7xxx alloys reported by several investigations [14,16–18]. The mechanism of PFZ formation is explained by the significant depletion in solute and/or vacancy concentration adjacent to the GBs during artificial aging [16,17,30,31]. It is believed that with Ag addition, the enhanced early Ag-vacancy and Ag-solute co-clusters ensure enhanced precipitation in the grain interior and adjacent to the GBs, which significantly decreases the width of the PFZ [16–18,32,33].

Studies on the role of minor Ag addition on corrosion behavior of 7xxx alloys are quite limited. Nevertheless, Ag has been reported to be beneficial in suppressing fatigue crack propagation [34] and resistance to stress corrosion cracking (SCC) [14,19,32,35]. SCC resistance with Ag addition was attributed to a narrower PFZ width and the partitioning of Ag in the GB η phase, making it more noble and lowering the potential difference in the GB region. These previous investigations mainly focused on 7xxx alloys with Zn/Mg of approximately 2 and did not investigate in detail the influence of Ag on localized corrosion and stress corrosion cracking behavior. Thus, the objective of this study is to go beyond the effect of Ag on enhanced cluster formation and age hardening response kinetics and systematically assess the precise impact of minor Ag addition on the microstructure evolution, mechanical and corrosion properties of a new generation 7xxx alloy with Zn/Mg of 4, using a range of materials characterization techniques and aqueous corrosion testing methods. The use of analytical methods such as (Scanning) transmission electron microscopy (S)TEM and Atom probe tomography (APT) facilitated a detailed characterization of the chemistry of precipitates, particularly after artificial aging. This enabled a strong correlation of the final microstructure with the mechanical properties, SCC and localized corrosion behavior, thus providing meaningful insights into potential future alloy chemistry modifications with Ag for high-strength, light weight design in the aviation/aerospace industry.

2. Material and methods

2.1. Materials and processing

The materials used for this investigation had compositions within the range of the commercial AA7449. In one alloy, ~0.4 wt% Ag was added using AlAg50 master alloy, and is herein referred to as 7449+Ag, while the base alloy is referred to as 7449. The alloys were cast in a Cu-mold as plates with dimensions (L × W × H) 185 mm × 145 mm × 100 mm. Prior to casting, the melt was purged with argon gas for 0.5 h to reduce the hydrogen content and ensure minimum porosity in the as-cast ingot. The actual composition of the alloys (in wt%) measured by optical emission spectrometry (OES) using a Hitachi High-Tech OE750 device is presented in Table 1.

Post-casting processing of the ingots proceeded with a two-step homogenization at 420 °C/5 h + 480 °C/24 h followed by hot rolling in multiple passes at a temperature of 400–460 °C to a final height of ~50 mm, which corresponds to a 50% height reduction. The rolled plates were solution heat treated at 480 °C for 2 h followed by quenching in water at room temperature to achieve the T4 temper. The samples were left at room temperature for a minimum of 3 days, followed by a two-step artificial aging at 121 °C/6 h + 163 °C/15 h to achieve the T76 condition.

2.2. Microstructure characterization

To pinpoint the precise role of Ag, a systematic approach was adopted to investigate the microstructure evolution of the alloys. Unless otherwise specified, samples for the bulk microstructure characterization were embedded in a cold-setting epoxy resin, ground using silicon carbide (SiC) paper, followed by polishing with diamond suspension and finally with SiO_2-based polishing suspension of 0.02 μm particle size. To characterize the grain size in the as-cast condition, the polished samples were etched for ~1.5 min using Barker's reagent, followed by imaging with polarized light by optical light microscopy (OLM) using a ZEISS Axio device. Grain size after processing was investigated by scanning electron microscopy (SEM) using a Zeiss Supra 55 VP (Carl Zeiss Microscopy, Germany) equipped with an electron backscatter diffraction (EBSD) detector from Oxford Instruments, UK. EBSD maps were collected with a step size of ~3.8 μm at an electron acceleration voltage of 20 kV and a working distance of 19 mm. To understand the coarse phases present in the as-cast condition and after processing, SEM energy-dispersive X-ray spectroscopy (EDX) was performed on polished samples. This was supported by phase evolution analysis by Differential Scanning Calorimetry (DSC) using a Linseis TG-DSC STP1750 device. DSC measurements were done on cylindrical samples of ~3 mm diameter and ~ 0.3 mm height, in argon atmosphere from room temperature (RT) to 650 °C and at a heating rate of 10 Kmin^{-1}. For the purpose of results reproducibility, three samples were used for each investigated alloy condition.

(Scanning) transmission electron microscopy (S)TEM was used to characterize the matrix and grain boundary precipitates (GBPs) present in the T4 and T76 conditions. Samples for TEM measurements were thinned in a solution of 25% HNO_3 and 75% CH_3OH at −30 °C by double jet electropolishing, using a Struers TenuPol 5 device. (S)TEM imaging was carried out using a JEOL JEM-F200 operated at an acceleration voltage of 200 kV and equipped with a GATAN oneView camera and an EDX detector from Oxford Instruments, UK. Precise characterization of the chemistry of the GBPs was done using the Cliff-Lorimer (CL) extrapolation of the matrix-influenced STEM-EDX results [36,37]. Atom Probe Tomography (APT) was employed to support precise chemistry characterization of precipitates and grain boundary segregation in the T76 condition. This was done by first identifying a marked high angle grain boundary (HAGB) from the EBSD maps, followed by the needle-shaped specimen preparation using a ThermoFisher Dual Beam Helios G4 Cxe plasma focused ion beam (Xe$^+$ pFIB) device. The sharpening of the needle-shaped specimen was done at a low acceleration voltage of 8 kV and a current decreasing from 1 nA to 10 pA as the needle became sharper, followed by a final cleaning step at an acceleration voltage of 5 kV and a current of 10 pA to remove potential implantation damage from the top layer. The APT analysis was performed on a Cameca LEAP 5000XR device at 70 K using the high voltage pulsing mode with a voltage pulse amplitude of 20%, a pulse repetition rate of 200 kHz and a detection rate of 0.4%. The 3D reconstruction [38] of the analyzed volumes, as well as the grain boundary and precipitate analysis, were

Table 1
Actual composition of alloys (wt%).

Alloys	Al	Zn	Mg	Cu	Zr	Ti	Fe	Si	Ag
7449	Bal.	8.40	2.04	1.97	0.12	0.02	0.08	0.04	–
7449+Ag	Bal.	8.30	1.99	1.94	0.12	0.02	0.08	0.04	0.38

carried out using the commercial software IVAS included in APSuite 6.1 (Cameca, USA). Solute clusters were identified using the isoconcentration surface which is based on local solute concentration. Atoms located in positions where the local solute concentration (for example Mg) is higher than a user defined threshold are filtered. This threshold is determined by calculating the binomial distribution in a random solid solution exhibiting the same elemental composition as the material of interest (the whole APT 3D reconstructed volume), and then, estimating the solute content value corresponding to 10% of the maximum frequency, which is, in our case, equal to ~2–3 at. %. This procedure allows to distinguish solute-enriched clusters (and precipitates) from simple composition fluctuations.

The frequently reported influence of Ag on age hardening kinetics was studied by electrical conductivity measurements and hardness tests in T4 condition, during artificial aging at 121 °C and after T76 aging. Electrical conductivity measurements were performed using a Sigma-Check 0.8.1 eddy current conductivity meter from ETHER NDE. Microhardness tests were performed using a Buehler MICROMET 5104 device with a test force of 0.5 kg (HV 0.5) and an indentation time of 15 s. An average of at least three measurements was taken for each heat treatment condition.

2.3. Slow strain rate test (SSRT) and localized corrosion test

The investigation of the influence of Ag addition on the stress corrosion cracking behavior was done by SSRT on smooth-round tensile samples using a Zwick Roell Kappa 100 DS. Samples were prepared such that the materials are loaded along the transverse direction. SSRT tests were performed at room temperature with a strain rate of 10^{-6} s^{-1} in an aerated 3.5% NaCl solution (pH ~6.2) under open circuit potential and in laboratory air as the reference environment. The calculation of the so-called SCC index (i_{scc}) which describes the susceptibility of the alloys to SCC was done by the ratio of the elongation-to-failure in NaCl (ε_{NaCl}) to the elongation-to-failure in air (ε_{Air}) according to Eq. (1) [39]. Fracture surfaces after SSRT were analyzed by SEM in secondary electron (SE) and backscattered electron (BSE) mode at an acceleration voltage of 15 kV.

$$I_{scc} = \frac{\varepsilon_{Air} - \varepsilon_{NaCl}}{\varepsilon_{Air}} \times 100\% \tag{1}$$

Pitting susceptibility in the SSRT solution of 3.5% NaCl was further investigated by potentiodynamic polarization (PDP) to access the impact of Ag addition on pitting susceptibility. PDP measurements were performed at 25 °C with a three-electrode set-up consisting of the alloys as the working electrode, saturated calomel electrode (SCE) as the reference electrode and a platinum sheet as the counter electrode. The samples were polarized from – 0.3 V to 0.3 V with respect to the open circuit potential at a scan rate of 0.17 mV/s using a Gamry® Reference 600 potentiostat, after 1 h stabilization at open circuit potential (OCP). This was supported by an intergranular corrosion (IGC) test according to ASTM G110 standard [40], in order to evaluate the grain boundary reactivity of the alloys. The samples for the IGC test had a dimension (L × W × T) of 40 mm × 20 mm × 2 mm. They were prepared in the long transverse (LT) – short transverse (ST) plane, to ensure IGC penetration occurs in the longitudinal (L) direction. Three samples were prepared for each alloy and test condition. To preserve the highly reactive precipitates, surface preparations were carried by water-free grinding with SiC paper to remove the surface oxides, followed by cleaning with acetone to remove any residue from the grinding process and drying in

air. Samples were weighed and then immersed for 6 h in a solution of 57 g NaCl +10 mL of 30% H_2O_2 per liter (pH ~5.9). For each sample, a solution volume of 150 mL maintained at a temperature of 30 °C was used. After the test duration, samples were removed from the solution, cleaned with running water to remove the corrosion products, followed by ethanol and dried. The samples were weighed after the test to determine the mass loss. Cross-sections were prepared by the metallographic procedures described in Section 2.2, followed by the imaging of the penetration depth by OLM and a more detailed characterization of the corrosion front by SEM. To support the mass loss and penetration depth results, the concentration of ions in the solution after the test was analyzed by Inductively Coupled Plasma Mass Spectrometry (ICP-MS) using a NexION 2000 spectrometer from PerkinElmer LAS GmbH, Germany. Prior to the ICP-MS analysis, the test solution was diluted by a ratio of 1:50 in 2% HNO$_3$.

3. Results

3.1. Grain structure

The results of the influence of Ag on the grain morphology and grain size in the as-cast condition and after processing are shown in Fig. 1. Both alloys show a dendritic equiaxed grain structure in the as-cast condition as can be seen in Fig. 1 (a) and (b). Interestingly, a larger average as-cast grain size of 569 ± 56 μm was observed in 7449+Ag compared with 7449, which had an as-cast grain size of 495 ± 49 μm.

The influence of Ag on the as cast grain size of 7xxx alloys has not been reported. A recent study [41] on an Al-33Zn-2Cu alloy showed as-cast grain refinement with up to 0.2 wt% Ag addition. However, the mechanism behind this was not explained. After processing to T4 condition, the dendritic structure was eliminated and the grains exhibit a 'pancake' structure aligned in the longitudinal direction as shown in the EBSD inverse pole figure (IPF) maps in Fig. 1 (c) and (d). The weighted average grain size by equivalent circle diameter is 383 ± 91 μm and 416 ± 92 μm for 7449 and 7449+Ag, respectively.

3.2. Eutectic and primary phase characterization

The SEM BSE images, the EDX results of the regions marked 1 and 2 and the corresponding element maps showing the eutectic and primary phases present in the alloys in the as-cast condition and after processing are shown in Figs. 2 and 3, respectively. In the as cast condition shown in Fig. 2 (a) – (o), the eutectic Mg(Zn,Cu,Al)$_2$ and Al$_7$Cu$_2$Fe phases were mainly identified in both the base alloy and the Ag-modified alloy. Similar to a previous study [42], Ag was found to be incorporated in the Mg(Zn,Cu,Al)$_2$ phase in 7449+Ag as shown in the EDX corresponding EDX point measurements. However, due to the overlapping of the EDX spectra of Ag Lα with 2(Al Kα) [43], the reported Ag amount in the eutectic Mg(Zn,Cu,Al)$_2$ phase might not be accurate. Although not shown in Fig. 2, Mg$_2$Si primary phase was equally present in both alloys in the as-cast condition, which is consistent with previous reports [3,44,45]. No additional phase was identified due to Ag addition by the SEM. After processing to the T76 condition as shown in Fig. 3(a) – (o), all of the coarse eutectic Mg(Zn,Cu,Al)$_2$ phase and the Ag-containing variant in 7449+Ag are dissolved and replaced by nano-sized precipitates (formed during artificial aging) which are not clearly visible in SEM. However, Al$_7$Cu$_2$Fe and Mg$_2$Si remain in the matrix and appear to have undergone spheroidization. SEM showed no additional coarse intermetallic phase with Ag addition.
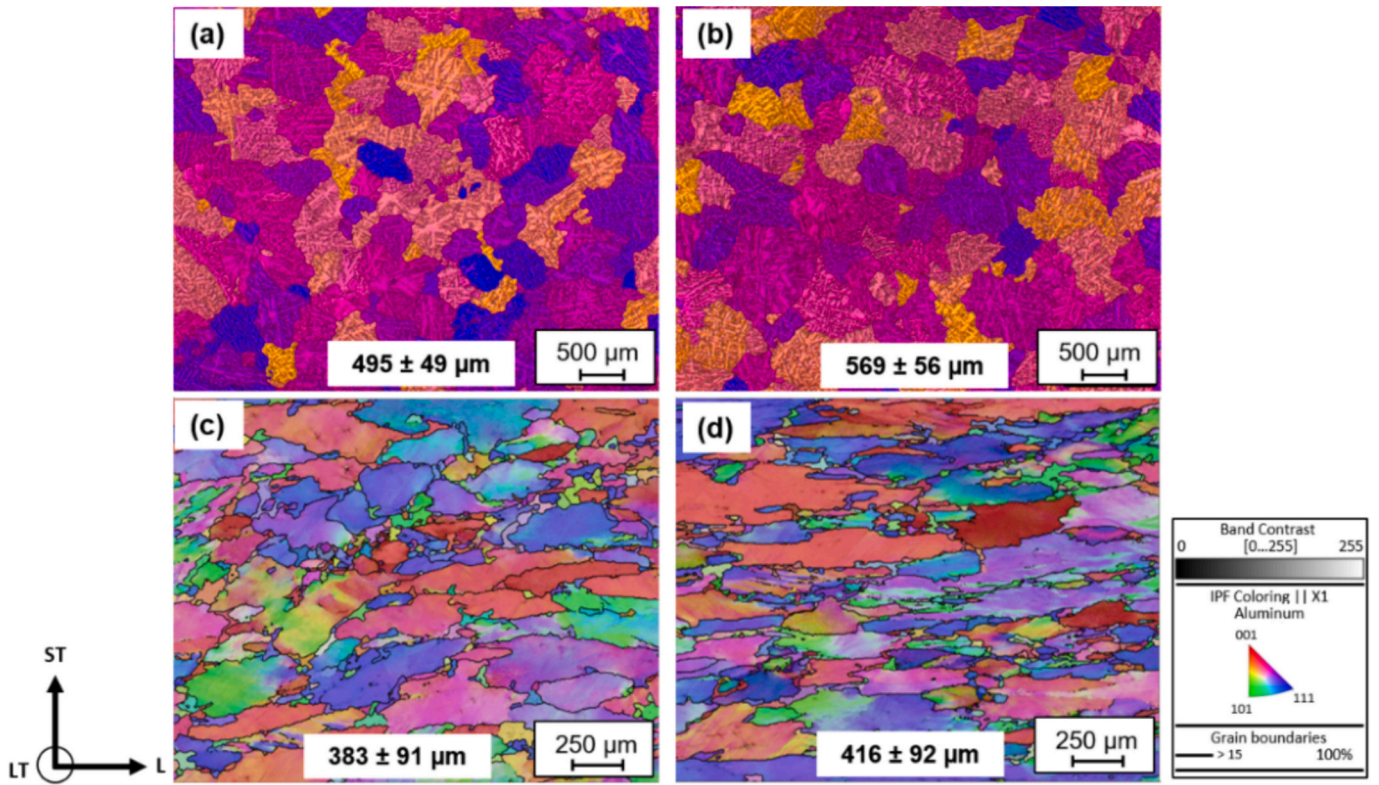
Fig. 1. Barker-etched images of the grains in as-cast condition (a) 7449 (b) 7449+Ag and EBSD IPF maps after processing to T76 condition (c) 7449 and (d) 7449+Ag.
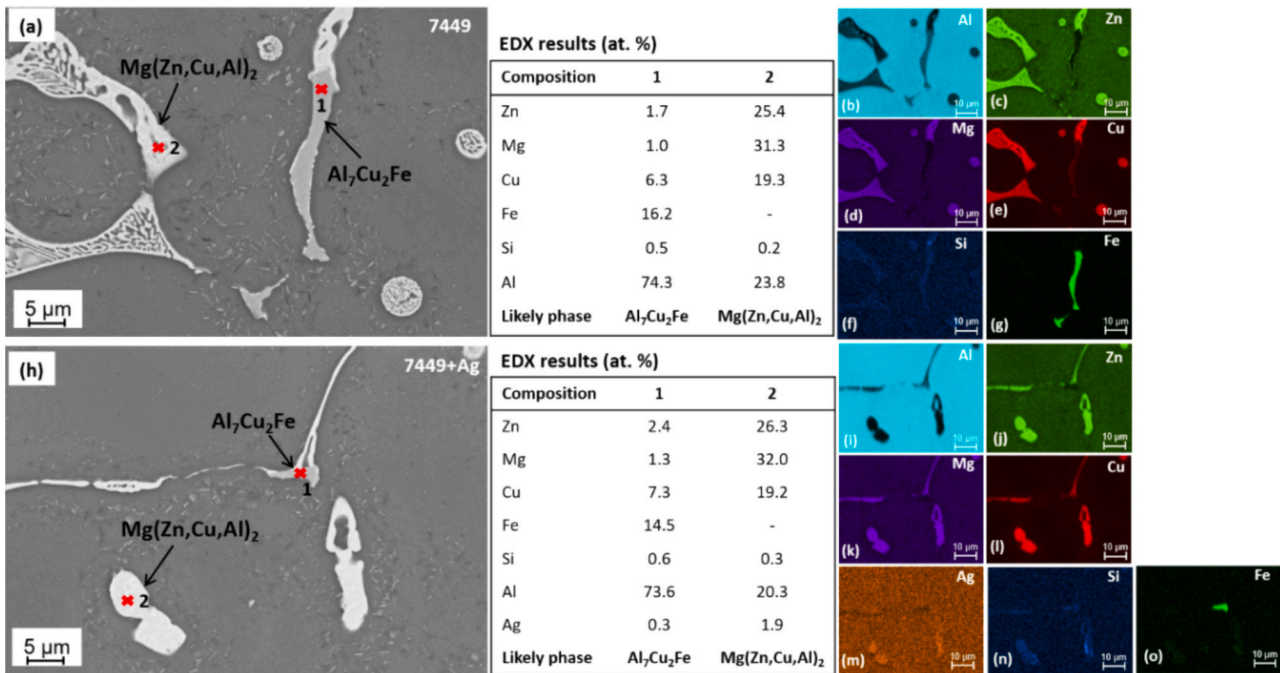

Fig. 2. SEM BSE images with the EDX results of region marked 1 and 2 and the corresponding element maps, (a) – (g) 7449 and (h) – (o) 7449+Ag showing the eutectic phases in the as-cast microstructure.

3.3. DSC analysis of phase evolution

Fig. 4 shows DSC results of the phase evolution in the as-cast, the T4 and the T76 conditions. In the as-cast condition as shown in Fig. 4(a), two endothermic peaks, labelled a and b, corresponding to the dissolution of the eutectic Mg(Zn,Cu,Al)$_2$ and the α-Al phase, respectively, were identified in both alloys. No distinct peaks for the dissolution of Al$_7$Cu$_2$Fe and Mg$_2$Si were identified, probably because of their overlap with the peak for the dissolution/melting of the α-Al phase. The red box represents the enlarged portion of the curve shown in Fig. 4 (b),
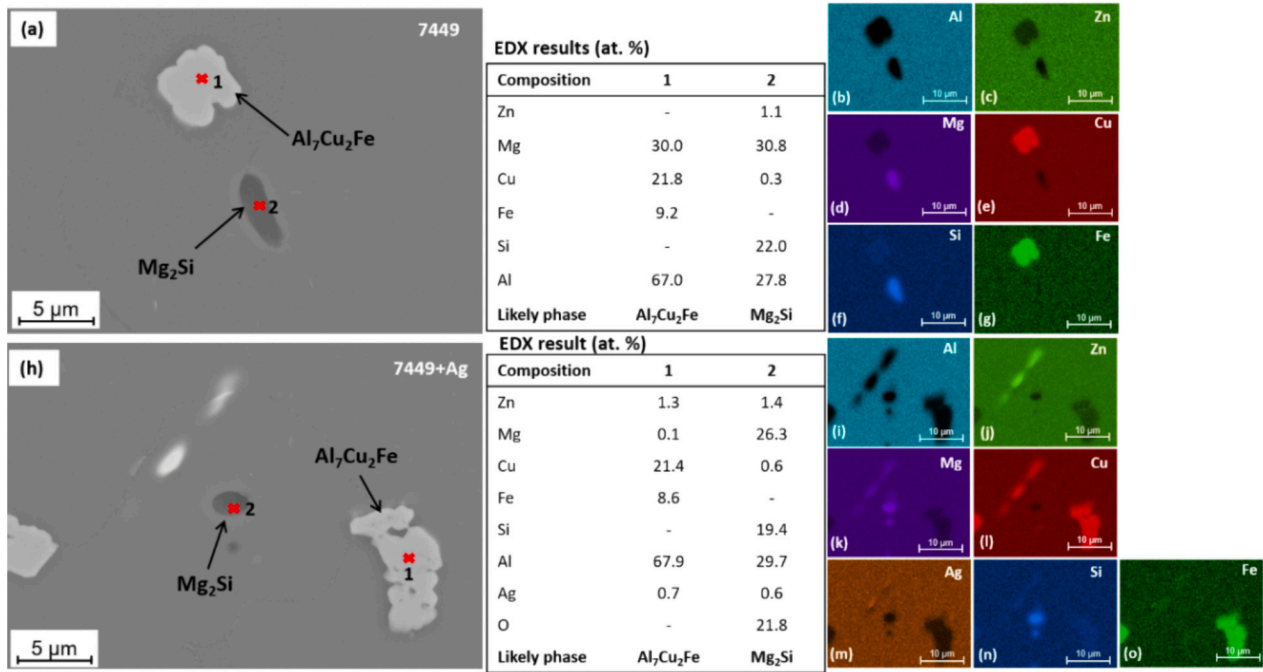
Fig. 3. SEM BSE images with the EDX results of region marked 1 and 2 and the corresponding EDX maps, (a) – (g) 7449 and (h) – (o) 7449+Ag showing the coarse intermetallics after processing to T76 condition.
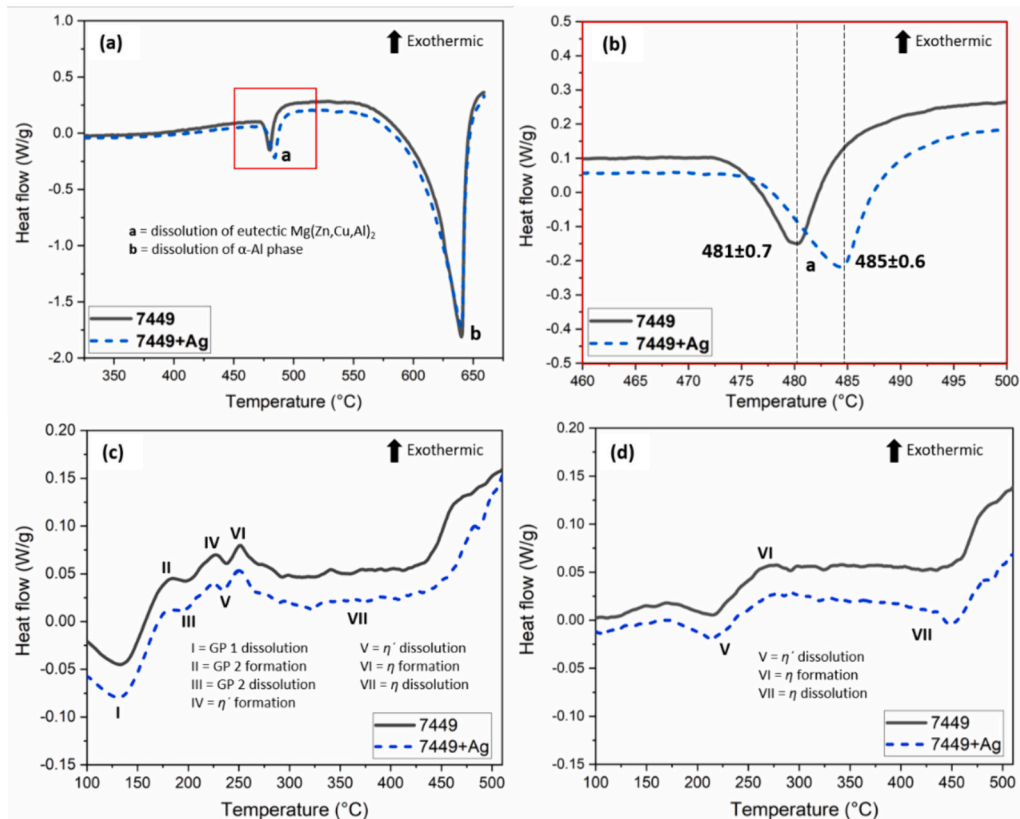

Fig. 4. DSC results showing phase evolution in alloys in different conditions: (a) as-cast condition (b) enlarged region in (a) indicated by red box (c) T4 condition and (d) T76 condition. (For interpretation of the references to color in this figure legend, the reader is referred to the web version of this article.)

where a clear shift in the position of the $Mg(Zn,Cu,Al)_2$ dissolution peak (a) from 481 °C in 7449 to 485 °C in 7449+Ag can be seen. This shift can be attributed to the presence of Ag in the eutectic $Mg(Zn,Cu,Al)_2$ phase.

Although such shifts of the eutectic phase to higher temperatures could necessitate a higher homogenization temperature, this was not the case in the present study since the incipient melting temperature of the phase

was ~478 °C in both alloys. Hence 480 °C was selected for the second step of the homogenization process in both alloys to avoid local melting.

After solution heat treatment (T4) condition as shown in Fig. 4 (c), four endothermic peaks I, III, V and VII identified at approximately 130 °C, 200 °C, 230 °C and 300–450 °C, respectively, and three exothermic peaks II, IV and VI identified at 175 °C, 225 °C and 250 °C, respectively, were observed in both alloys. Peak I corresponds to the dissolution of mainly GP (I) zones formed at RT and probably during the DSC measurement [23,46–49], while Peak II and III correspond to GP (II) zones formation and dissolution/transformation to η´, respectively [47,50]. Peaks IV and V are due to the precipitation and dissolution of the metastable η´ phase. The exothermic peak VI is related to the formation of the equilibrium η phase while the broad endothermic peak VII corresponds to its dissolution [48,49,51]. No change in the peak positions and no additional peak were identified in the Ag-modified alloy. After T76 aging, only peaks V, VI and VII were identified in both alloys, suggesting the prior existence of η´, the additional formation of η phase and its subsequent dissolution. No peak corresponding to T phase was identified. These results, particularly in the T4 condition agrees with the know precipitation sequence of [23,52]: $SSSS \rightarrow GP\ zones \rightarrow \eta´ \rightarrow \eta - Mg(Zn, Cu, Al)_2$.

3.4. TEM characterization of matrix microstructure

Conventional bright field (BF) TEM images and their corresponding selected area electron diffraction (SAED) patterns (indexed for Al) of the alloys in the T4 condition are shown in Fig. 5. BF-TEM images in Fig. 5 (a), (d) for 7449 and 7449+Ag, respectively, show the presence of Al_3Zr dispersoids in the matrix. These were confirmed by the SAED patterns as spots at the $1/2\ \{220\}_{Al}$ position which corresponds to the forbidden $\{110\}_{Al}$ positions when viewed along the $[\bar{1}14]_{Al}$ and $[\bar{1}12]_{Al}$ zone axes [5,25,53], as shown in Fig. 5(b), (c) and (e), (f) for 7449 and 7449+Ag, respectively. Although not shown at the magnification of the BF-TEM images, diffraction spots related to GP (I) and GP (II) zones are present in the T4 condition as shown in the SAED patterns. GP (I) zones are solute clusters formed from RT – 150 °C after solution treatment, while GP (II) zones are vacancy-rich clusters with Zn-rich layers formed during rapid quenching from a solution treatment temperature above 450 °C,

which explains their presence in the T4 microstructure [24,25,47,51]. No strong diffraction spots related to GP zones were identified in the $[\bar{1}12]_{Al}$ projection. However, in the $[\bar{1}14]_{Al}$ projection, GP (I) zones were identified as weak diffuse spots at $\{1, 3/4, 0\}$ position [49] while GP (II) zones were observed as irregular-shaped spots close to $1/2$ $\{113\}_{Al}$ which is similar to the observation in the $[112]_{Al}$ projection [24,47,54]. This indicates that despite some GP (II) zones formation from the T4 condition as indicated by the shallow exothermic peak II in the DSC measurements in Fig. 4 (c), they are equally formed during quenching from the solution treatment temperature in these alloys. Furthermore, a Ag-rich phase believed to be AlAgZnMgCu phase with a diameter of 15–35 nm, which was not visible in the SEM, was equally observed in 7449+Ag in T4 condition as shown in the BF-TEM image in Fig. 5(d). This phase showed a strong Ag enrichment, as shown in Fig. 6, making it distinguishable from the Al_3Zr dispersoids. No additional diffraction spot corresponding to this phase was identified along the $[\bar{1}14]_{Al}$ and $[\bar{1}12]_{Al}$ zone axes. Further analysis of this phase by high-resolution TEM (HRTEM) and STEM – EDX as are shown in Fig. 6.

The HRTEM image of the AlAgZnMgCu phase (red box in Fig. 5(d)) and the corresponding Fast Fourier Transform (FFT) are shown in Fig. 6 (a) and (b), respectively.

Three lattice (d) spacings of the AlAgZnMgCu phase, namely; $d_1 = 6.2$ Å, $d_2 = 3.5$ Å and $d_3 = 2.3$ Å, were measured as indicated in the inverse FFT (IFFT) images shown in Fig. 6(c) – (e) of the orange box in Fig. 6 (a). The IFFT image of the interface (blue box) in Fig. 6(f) shows minor misfit dislocations, indicating that this phase might be non-coherent with the matrix. The dark field (DF) STEM image and the corresponding EDX quantification results shown in Fig. 6(f) and (g), respectively, suggest a significant enrichment of Ag in the phase. The precise stoichiometry of this phase is unknown due to the possibility of bulk Al-matrix contribution during the measurements. The AlAgZnMgCu phase is believed to have formed due to a decrease in the solubility limit of Ag resulting from the presence of Mg and the high Zn content of the alloy, as proposed by Polmear [14,30]. This phase could be related to the AlAgZn type phase with a hexagonal (HCP) structure (space group $P6_3/mmc$) and lattice parameters a = 2.885 Å and c = 4.662 Å [30]. Also, a calculation of the d-spacings from these lattice constants for the HCP crystal structure gives 2.3 Å for a (0002) plane,
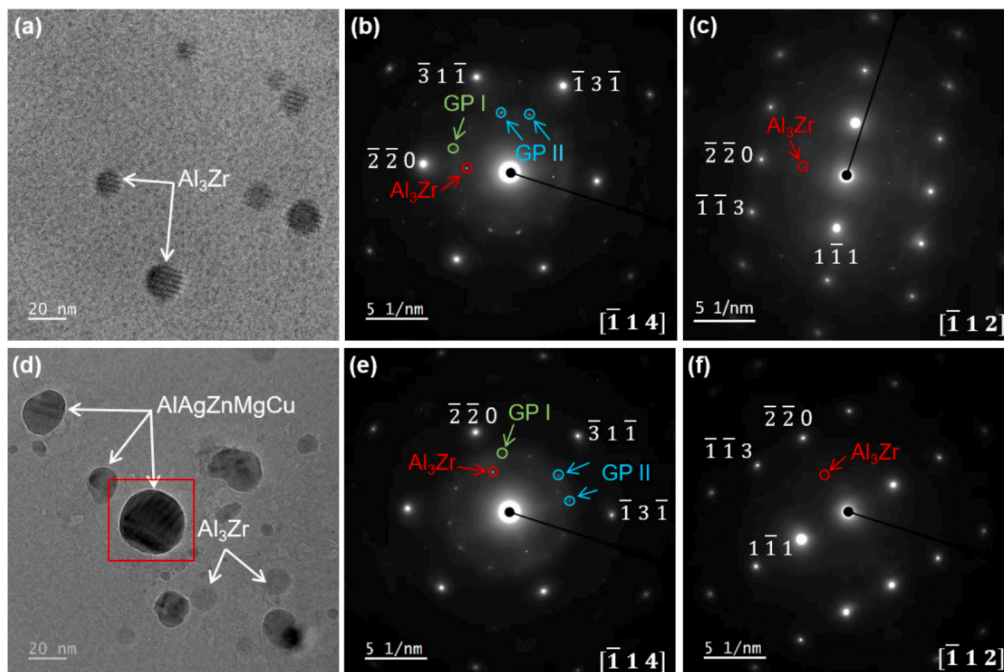

Fig. 5. BF-TEM image and corresponding SAED patterns in T4 condition taken along the $[\bar{1}14]_{Al}$ and $[\bar{1}12]_{Al}$ zone axes, (a) – (c) 7449 and (d) – (f) 7449+Ag.
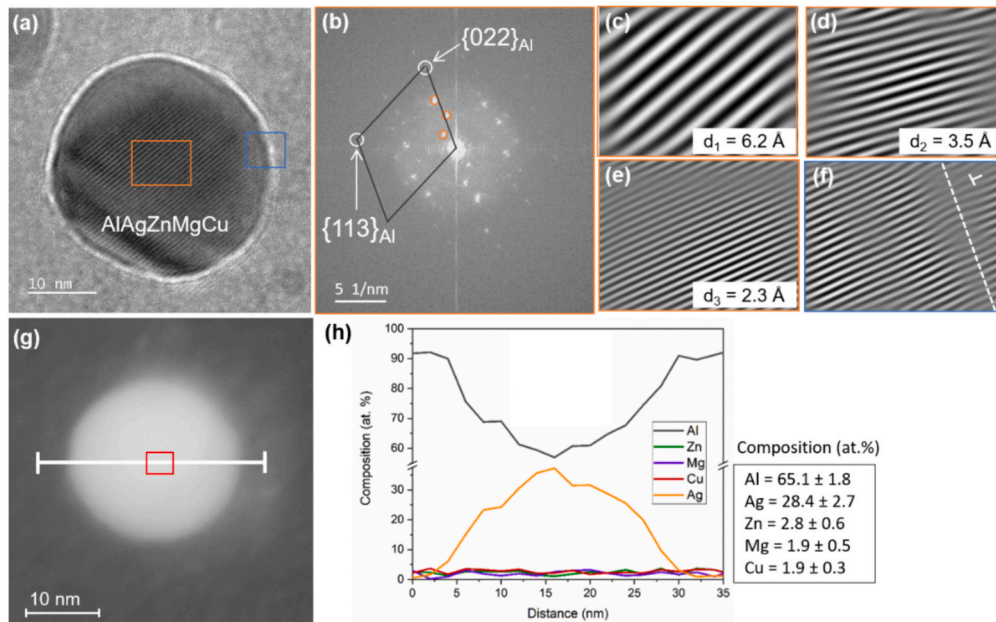
Fig. 6. (a) HRTEM image of AlAgZnMgCu phase highlighted by the red box in Fig. 5 (d) (b) Corresponding FFT pattern (c) – (f) IFFT images showing measured d spacings (orange box) and misfit dislocation at the interface (blue box) (g) DF-STEM image of the phase and (h) EDX line scan and quantification result of the region marked by the red box. (For interpretation of the references to color in this figure legend, the reader is referred to the web version of this article.)

which is equal to the measured d_3.

BF-TEM images and their corresponding SAED patterns (indexed for Al) of the matrix microstructure of the alloys in the T76 condition are shown in Fig. 7. As expected after T76 aging, several nano-sized, elongated precipitates with length of 5–20 nm and width of 1–5 nm were present in the matrix of the alloys as shown in Fig. 7(a), (d) for 7449 and 7449+Ag, respectively. No obvious growth of the AlAgZnMgCu phase was observed.

The nano-sized precipitates are believed to be the elongated/platelet-type η'/η precipitates and were confirmed by the SAED patterns taken along the $[\bar{1}14]_{Al}$ and $[\bar{1}12]_{Al}$ zone axes. In the $[\bar{1}14]_{Al}$

projection shown in Fig. 7(b), (e) for 7449 and 7449+Ag, respectively, diffraction spots of η' were identified at the $1/3$ and $2/3$ position of the $\{220\}_{Al}$ plane, which is consistent with previous observations [25,49,52,55]. Furthermore, in the $[\bar{1}12]_{Al}$ projection shown in Fig. 7 (c), (f) for 7449 and 7449+Ag, respectively, "streaks" from multiple diffraction spots of η'/η precipitates were identified at the $(10.l)_{\eta'/\eta}$ and $(20.l)_{\eta'/\eta}$ positions [25,52]. The diffraction spots identified outside of $\{220\}_{Al}$ and $\{113\}_{Al}$ planes in Fig. 7(f) for 7449+Ag are related to the η precipitate [25].
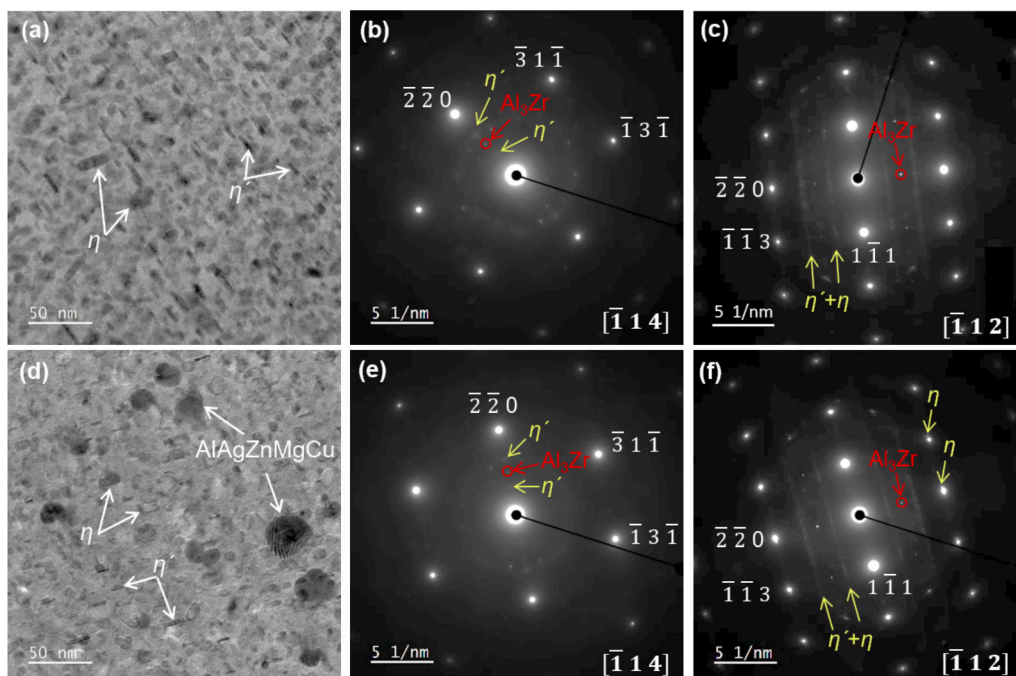

Fig. 7. BF-TEM image and corresponding SAED patterns in T76 condition taken along the $[\bar{1}14]_{Al}$ and $[\bar{1}12]_{Al}$ zone axes, (a) – (c) 7449 and (d) – (f) 7449+Ag.

3.5. TEM characterization of GBP chemistry

The results of the GBP chemistry in T4 and T76 conditions are shown in Figs. 8 and 9, respectively. In the T4 condition, DF-STEM images and their corresponding EDX maps shown in Fig. 8(a) – (e) for 7449 and in (f) – (k) for 7449+Ag show some of the GBs which are sparsely populated by the η-Mg(Zn,Cu,Al)$_2$ phase. These are believed to have formed during quenching from the solution treatment temperature and had a size of 80–280 nm in 7449 and 20–30 nm in 7449+Ag. Ag has been proposed to promote cluster formation in the matrix by trapping vacancies and solute atoms diffusing to the GBs and suppressing GB precipitation [12,14,17,32,33]. In the T76 condition, DF-STEM images and their corresponding EDX for 7449 (Fig. 8(a) – (e)) and 7449+Ag (Fig. 8(f) – (k)) show an increase in the width of the GBPs and the area coverage of the GBs. The presence of a PFZ is also visible. However, no decrease in the width of the PFZ was observed in 7449+Ag, which is contrary to previous observations in Al-Zn-Mg and Al-Zn-Mg-Cu 7xxx alloys with Zn/Mg of ~2 [16–18,33]. The GBPs chemistry from the Cliff-Lorimer extrapolation of the EDX results was determined by fixing the Mg content at 33 at. % [37,56]. In the T4 condition as shown in Fig. 8(l) and (m) for 7449 and 7449+Ag, respectively, Ag of ~3 at. % was measured in the GBPs in 7449+Ag, where they seem to substitute Cu or Zn. A similar observation was made in T76 condition (Fig. 9(l) and (m)), with the GBPs having ~2 at. % Ag in 7449+Ag, with minor deviations in Zn and Al relative to 7449. Furthermore, the Cu content of the GBP (quenching-induced) in T4 condition was higher than in the T76 condition.

3.6. APT results of precipitate chemistry and GB segregation

The APT images of the alloys in T76 condition (Fig. 10) show differences in the morphology of the matrix precipitates which were not discernible by TEM (Fig. 7) in both alloys. Fig. 10(a) and (b) show the 3D reconstructed volumes with the individual element enrichments in precipitates in 7449 and 7449+Ag, respectively. Fig. 10 (c) and (d) are presented to confirm the position of the GB in (a), since the much smaller enrichment could be misconstrued as matrix precipitation. In the base alloy, the matrix precipitates (MPs) mainly had a spherical morphology with an average diameter of 6 ± 3 nm and a volume fraction (fv) of 5.9%. However, in the 7449+Ag alloy, the APT showed both spherical precipitates with an average diameter of 4 ± 1 nm and predominantly the rod-shaped precipitates with an average length of 13 ± 6 nm and thickness of 5 ± 1 nm. A comparable MPs fv of 5.4% was determined for the Ag-modified alloy. The spherical precipitates in both alloys are believed to be the η'/η_2 plates on the {111}$_{Al}$ lattice, while the elongated precipitate in 7449+Ag could be a different variant of the η'/η_2 precipitates [54,57,58]. From the chemistry perspective, the partitioning of the major alloying elements Zn, Mg and Cu in the MPs, GBs and in the GBP (in 7449+Ag) was observed. In Fig. 10 (b) for 7449+Ag, Ag was found to be incorporated in the MPs and GBP, but depleted along the GB. The presence of Ag in the precipitates implies that some amount of Ag was present in solid solution and in GP zones during artificial aging, and not entirely segregated in the AlAgZnMgCu phase. The arrows show the regions of interest for the 1D composition profiles in Fig. 11 and the chemistry results of the MPs, GB segregation and the GBP (in 7449+Ag) in Table 2.

The 1D composition profiles for the MPs in 7449+Ag shown in Fig. 11(c) are for the rod-shaped precipitates. According to the results reported in Table 2, the Mg and Cu contents of the spherical MPs in both alloys are quite similar. A slightly higher Zn content was measured in the spherical MPs in 7449, giving an average Zn/Mg ratio of 1.4 compared with a Zn/Mg ratio of 1.1 determined for 7449+Ag. These results are within the Zn/Mg ratio of 1.2–1.3 reported for η' platelets [54,59]. Furthermore, Ag of ~1 at. % is incorporated in these particles, which agrees with an earlier investigation on 7075+Ag after aging at 150 °C
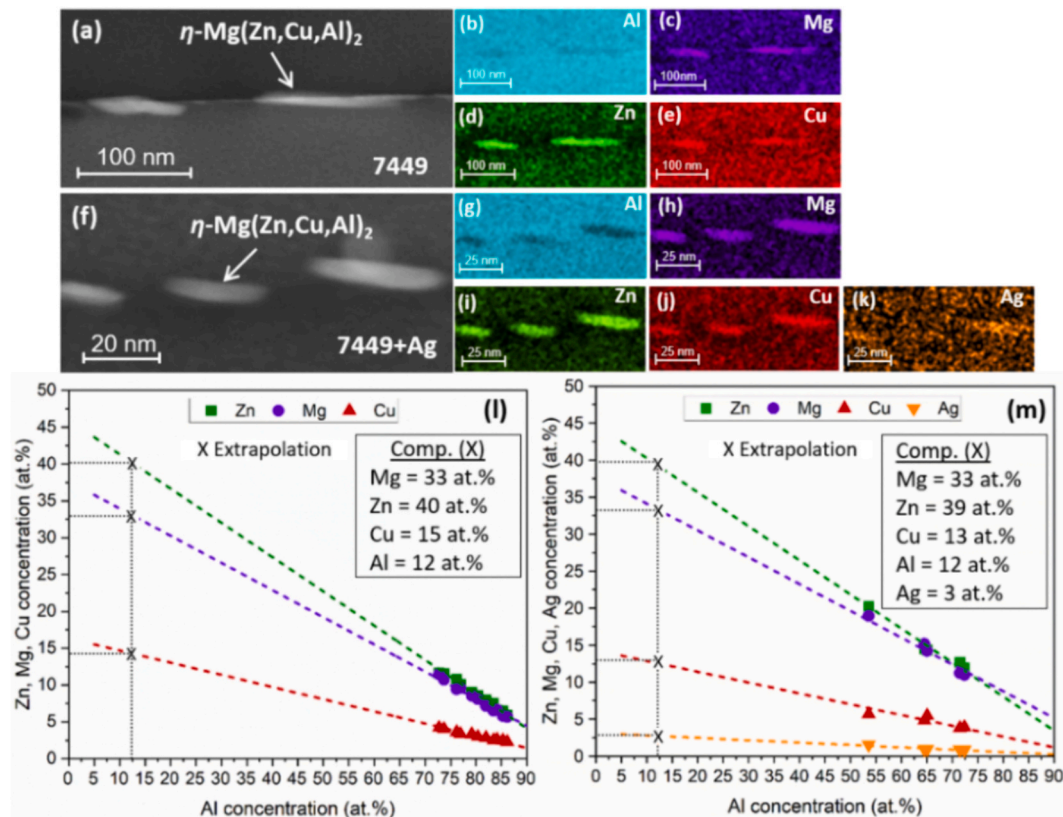

Fig. 8. DF-STEM images and their corresponding EDX maps in T4 (a) – (e) 7449 and (f) – (k) 7449+Ag. The Cliff-Lorimer extrapolation results are shown in (l) and (m) for 7449 and 7449+Ag, respectively.
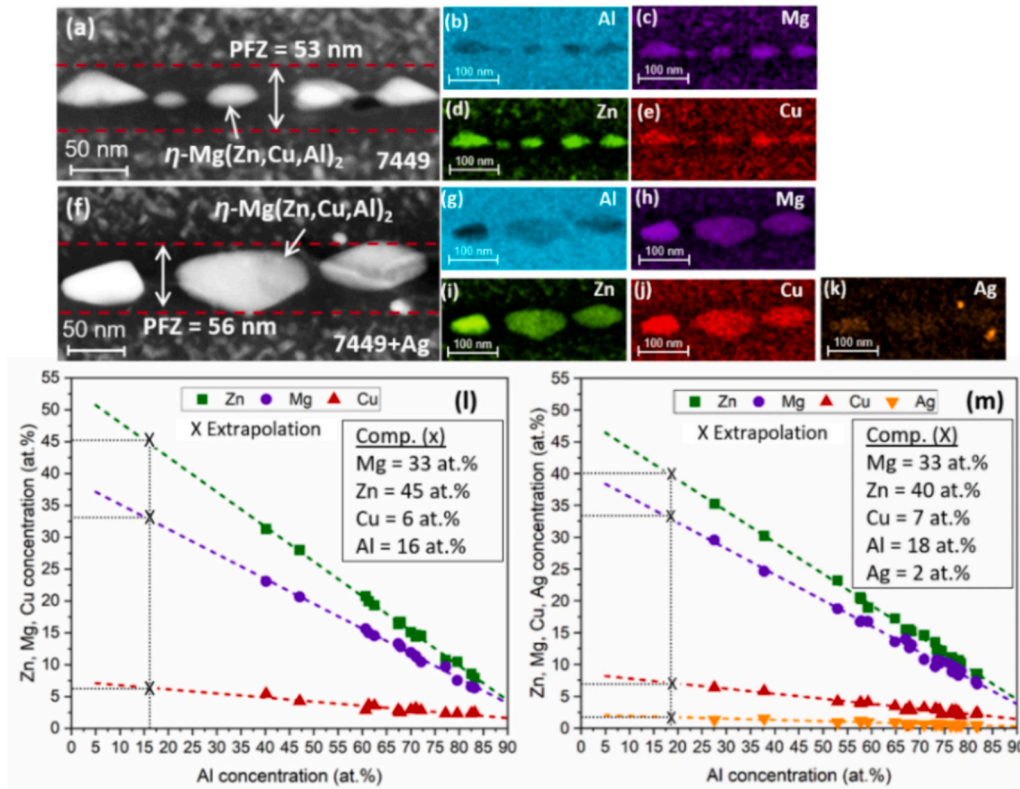
Fig. 9. DF-STEM images and their corresponding EDX maps in T76 (a) – (e) 7449 and (f) – (k) 7449 + Ag. The Cliff-Lorimer extrapolation results are shown in (l) and (m) for 7449 and 7449 + Ag, respectively.
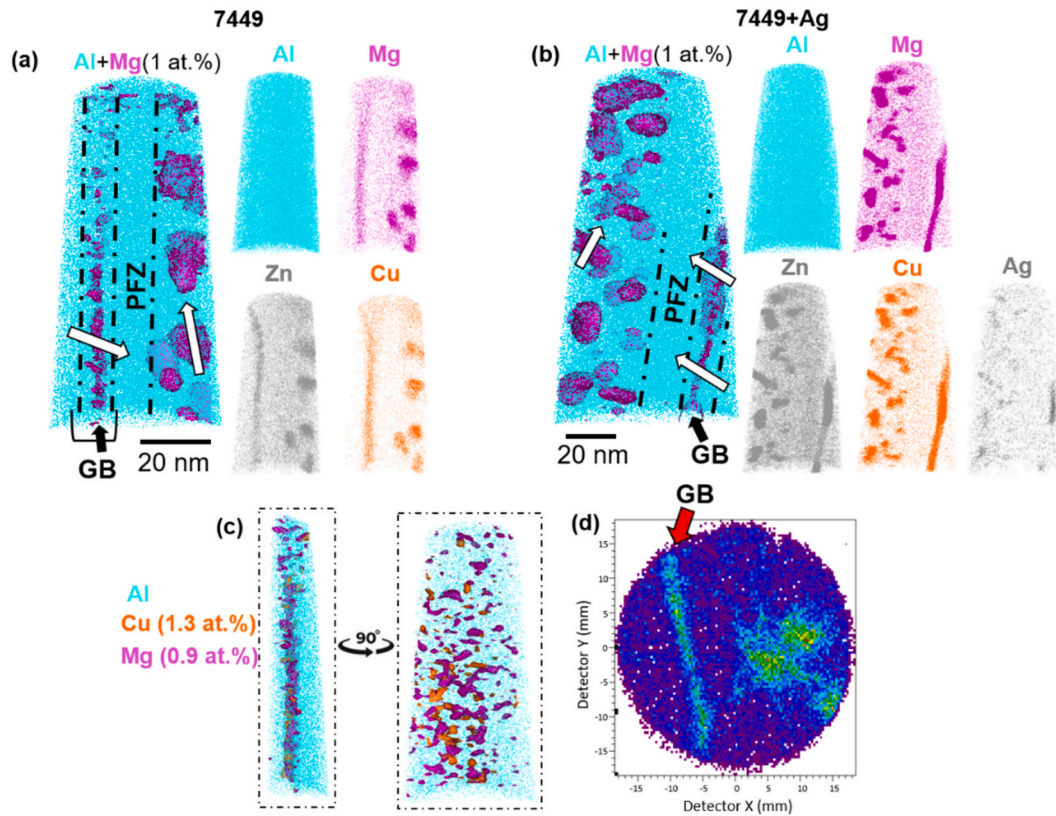

Fig. 10. 3D reconstructed volumes of APT samples showing microstructural features highlighted with respect to 1 at. % isosurfaces (Mg) and element distributions (Al, Mg, Zn, Cu and Ag) in precipitates and GB segregation in T76 condition (a) 7449 and (b) 7449+Ag. (c) shows the GB region in (a) and at 90° rotation confirming the observed GB enrichment as solute segregation. The detector events histogram showing the density of events and confirming the GB position is presented in (d).
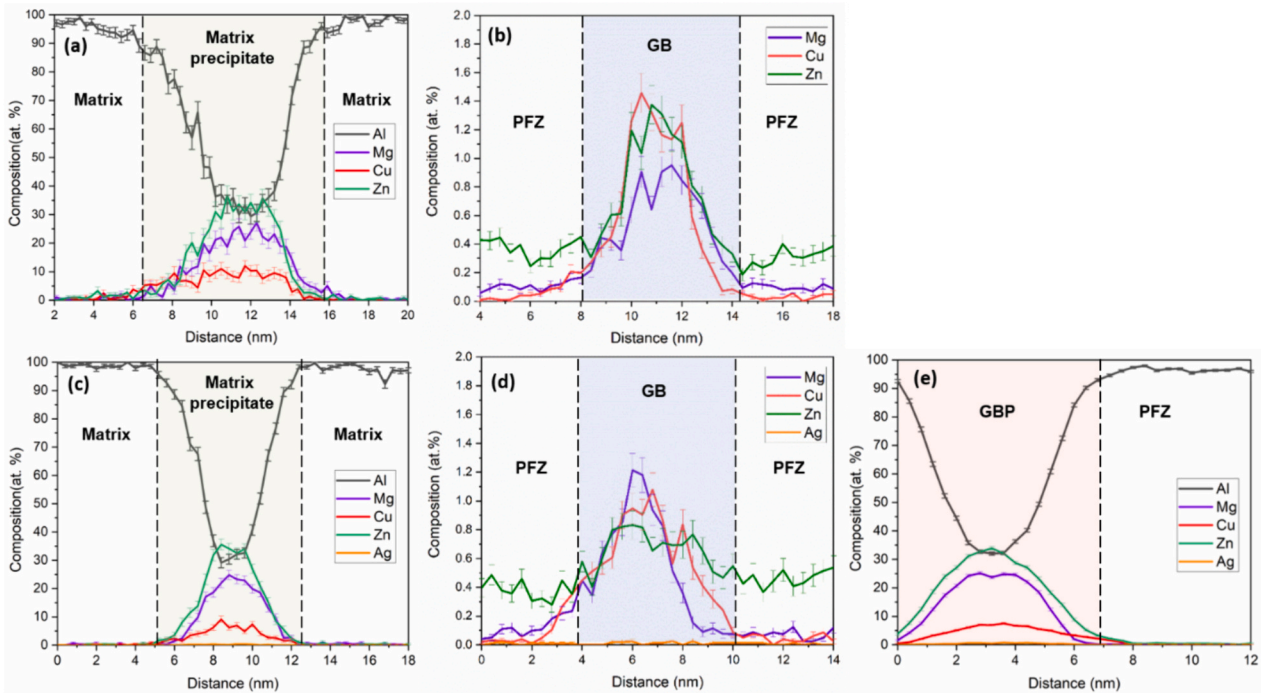
Fig. 11. 1D composition profiles, measured by APT across matrix precipitates (a) 7449 (c) 7449+Ag, GB segregation (b) 7449 (d) 7449+Ag and GBP in 7449+Ag (e) (For interpretation of the references to color in this figure, the reader is referred to the web version of this article).

Table 2
Mean value (at. %) of the chemical composition of precipitates and GB segregation in T76 condition measured by APT.

Alloy	Feature	Zn	Mg	Cu	Ag	Al
7449	Spherical MPs	33 ± 2.3	24 ± 0.3	9 ± 1.2	–	Bal.
7449+Ag	Spherical MPs	25 ± 5.5	23 ± 1.5	10 ± 3.1	1.0 ± 0.1	Bal.
	Rod-shaped MPs	41 ± 8	26 ± 2.7	6 ± 0.8	0.5 ± 0.2	Bal.
	GBP	40 ± 0.6	30 ± 0.5	8 ± 0.3	0.9 ± 0.1	21 ± 0.4
7449	GB segregation	1.2 ± 0.04	0.7 ± 0.03	0.9 ± 0.03	–	–
7449+Ag	GB segregation	0.8 ± 0.03	0.9 ± 0.03	0.8 ± 0.03	0.01 ± 0.004	–

for 50 h [18]. On the other hand, the elongated rod-shaped MPs in 7449+Ag had a comparable Mg amount with the spherical MPs. However, a lower Cu, Ag and a much higher Zn content was measured, resulting in a Zn/Mg ratio of 1.6. This suggests a different type of η'/η in 7449+Ag, as indicated by the additional diffraction spots in SAED pattern in Fig. 7(f) and reported by Stiller et al. [54].

The results obtained regarding the GB segregation (Fig. 11 (b), (d)) and reported in Table 2 show no significant difference in the segregation amount of Zn, Mg and Cu (maximum segregation level of ~1 at.%) in the T76 condition. This indicates a strong decrease in the segregation levels after solution heat treatment, which has been previously reported to be ~4.5 at. % for Zn and Mg and 1.6 at.% for Cu in an Al-6.2Zn-2.5Mg-2.1Cu alloy [56]. No Ag segregation at the GB in 7449+Ag was observed. Also, similar amount of solutes in the PFZ was measured in both alloys. Furthermore, the composition of Zn, Mg, Cu and Al in the GBP precipitate (Fig. 11(e)) shown in Table 2 was found to be very close to that estimated from the STEM-EDX results in Fig. 9(m), suggesting a good agreement of both methods. However, the Ag content was slightly over estimated by 1 at. % by the STEM-EDX.

3.7. Hardness and conductivity measurements

The results of the influence of Ag on the age hardening response measured by Vickers microhardness test and electrical conductivity measurements are shown in Fig. 12. In the T4 condition, 7449+Ag showed a slightly higher hardness and electrical conductivity of about 3% with respect to the base alloy. This observation can be attributed to the increase in the density of clusters/GP zones during natural aging in the 7449+Ag alloy [13,14,21,22] and the presence of the AlAgZnMgCu phase, shown by the TEM results in Fig. 5. However, contrary to previous reports on Al-Zn-Mg and Al-Zn-Mg-Cu alloys with Zn/Mg ratio of ≤2 [13,14,17,18,20–22], Ag addition in 7449 did not show an enhanced age hardening response during artificial aging at 121 °C and after T76 aging. In fact, the Ag-modified alloy showed a slightly lower hardness and comparable conductivity with the base alloy after T76 aging
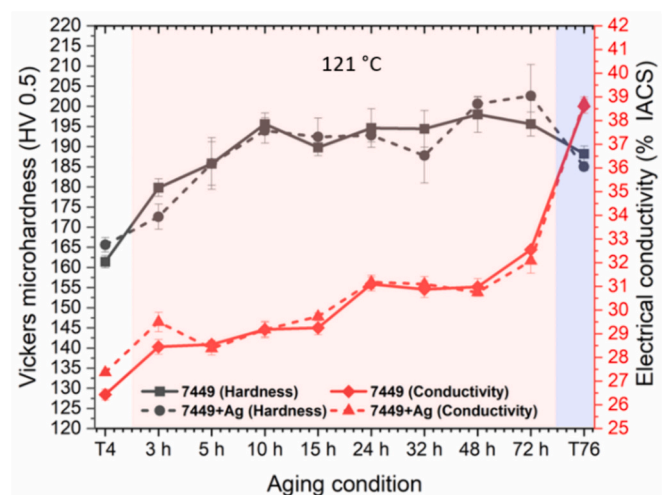

Fig. 12. Vickers hardness test and electrical conductivity results showing age hardening response.

treatment. This may be due to the presence of the AlAgZnMgCu particles in the matrix of 7449+Ag after T76 aging, which are relatively larger than the strengthening η'/η precipitates that are mainly present in the matrix of the base alloy as shown in Fig. 7.

3.8. SSRT test and fracture surfaces

Fig. 13(a), (b) shows the stress-strain curves from the SSRT test in T4 and T76 conditions, respectively. In the reference (air) environment as shown in Fig. 13 (c), a slightly higher yield strength ($\sigma_{0.2}$) and ultimate tensile strength (σ_m) were measured in 7449+Ag relative to 7449 in the T4 condition. The 7449 alloy showed a $\sigma_{0.2}$ of 357 $\pm$ 2 MPa and a σ_m of 478 $\pm$ 12 MPa, which increased to 401 $\pm$ 5 MPa and 504 $\pm$ 6 MPa, respectively after Ag addition. This observation is consistent with the hardness and conductivity results, where higher values were measured in 7449+Ag in the T4 condition, indicating an enhanced response to natural aging. However, this increase in strength was to the detriment of ductility (Fig. 13(d)), with 7449+Ag having a lower elongation to failure (ε) of 8 $\pm$ 1% compared to 10 $\pm$ 1% for 7449. Again, similar to the hardness and conductivity results, Ag addition did not show an increase in strength after T76 aging. A $\sigma_{0.2}$ of 542 $\pm$ 4 MPa and a σ_m of 560 $\pm$ 4 MPa were measured in the 7449 alloy, while the Ag-modified alloy showed a slightly lower $\sigma_{0.2}$ of 531 $\pm$ 13 MPa and a σ_m of 552 $\pm$ 11 MPa. In terms of ductility after T76 aging (Fig. 13(d)), a slightly lower elongation to failure (ε) of 6 $\pm$ 1% was determined in 7449+Ag compared to 7 $\pm$ 1% measured in the base alloy.

These results are consistent with a previous study [29] where lower strengths and elongation were reported with 0.2 wt% Ag addition in an Al-8Zn-1Cu-1.3Mg-0.1Zr alloy after T77 aging treatment. As expected, the tests in a 3.5% NaCl solution under OCP showed a loss in ductility (ε) relative to the tests in air in both alloys and in T4 and T76 conditions. Furthermore, a minor increase in the $\sigma_{0.2}$ and σ_m was observed in T4.

The I_{scc} calculated from the Eq. (1) are inserted in Fig. 13 (d). In the T4 condition (with higher I_{scc} compared to T76), Ag addition did not show any effect on the SCC sensitivity, with both alloys having an I_{scc} of 74%. However, after T76 aging, 7449+Ag showed a higher SCC susceptibility (I_{scc} = 33%) compared to the base alloy (I_{scc} = 24%).

SEM images of the fracture surfaces of the samples tested in NaCl solution are shown in Fig. 14. The samples showed several regions of brittle SCC which are highlighted by the red dashed lines in the overview images in Fig. 14 (a), (c) and (e), (g), followed by regions of ductile overload fracture. Fig. 14 (b), (d) and (f), (h) for 7449 and 7449+Ag in T4 and T76, respectively, represent the regions marked by the blue boxes. In the T4 condition, both alloys show a combination of intergranular SCC (IGSCC) and cleavage-like transgranular SCC (TGSCC) mainly at the rim zone, with the former dominating. Grain boundary gaps (yellow arrows) were also observed in both alloys in the T4 condition. After T76 aging, TGSCC was mainly observed, indicating a decrease in the sensitivity of the GB region to SCC propagation. No change in the fracture mode with Ag addition was observed. Both IGSCC [60–62] and cleavage-like TGSCC [7,63–66] fracture modes have been reported in 7xxx alloys after mechanical tests in NaCl solution, and are believed to result from hydrogen absorption, diffusion and trapping at microstructural features. Diffusion and trapping of hydrogen atoms at microstructural features ahead of a crack tip can result in the brittle fracture of a ductile material. The proposed mechanisms of hydrogen embrittlement phenomena and mechanisms in Al include Hydrogen Enhanced Decohesion (HEDE), Hydrogen Enhanced Localized Plasticity (HELP) or by Adsorption-Induced Dislocation Emission (AIDE) [62,67]. These mechanisms are discussed in the next chapter.

Fig. 15 and Table 3 show the results of the PDP measurements. The initial OCP (Fig. 15 (a)) shows potential stabilization over time, prior to PDP. Table 3 indicates that Ag addition did not influence the OCP in T4 and T76 conditions. However, considering the two aging conditions, the
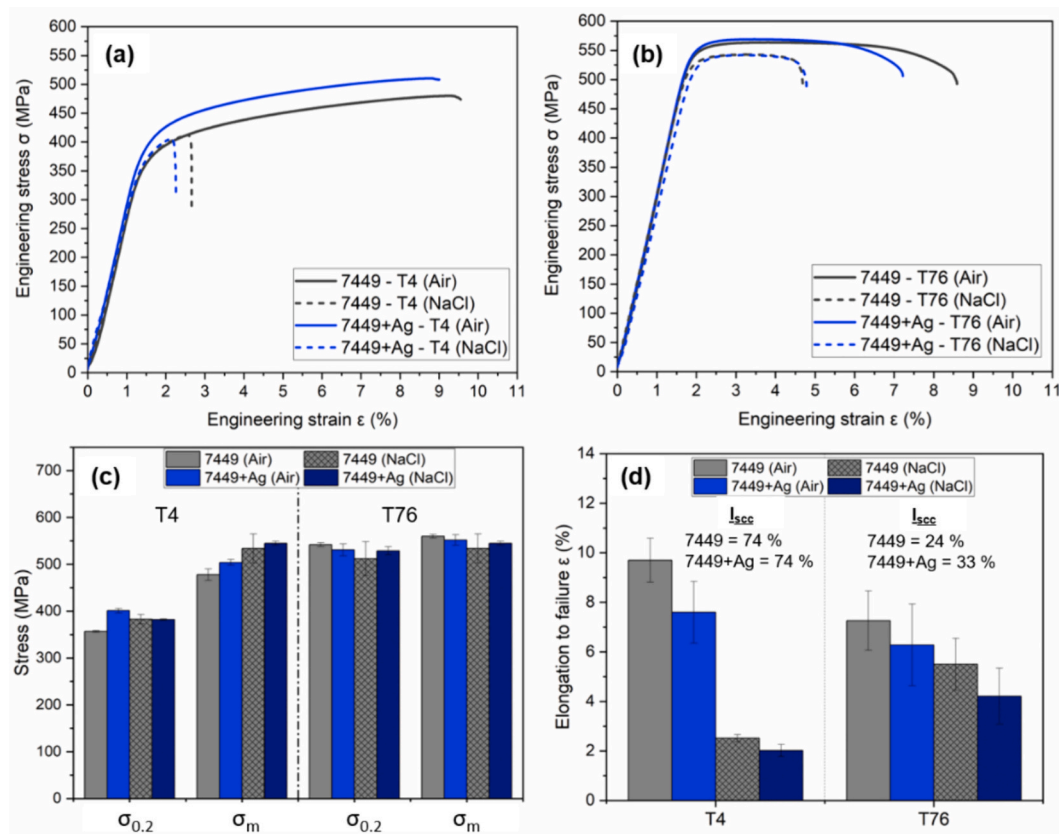

Fig. 13. Stress-strain curves (SSRT) showing the mechanical properties in air and in 3.5% NaCl solution in (a) T4 and (b) T76. The strength (σ) and maximum elongation (ε) are shown in (c) and (d), respectively. The calculated I_{scc} in T4 and T76 conditions are shown in (d).
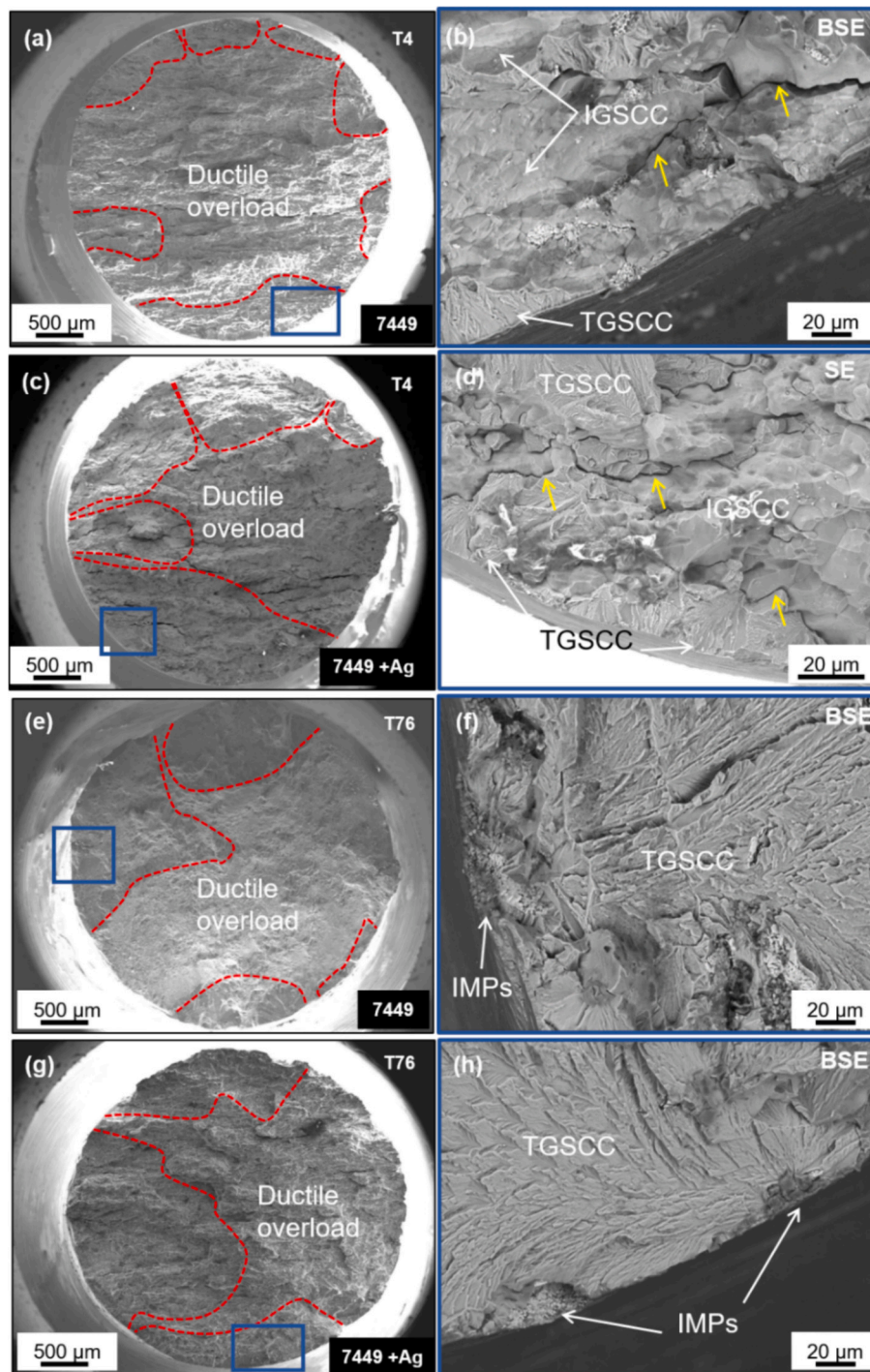
Fig. 14. SEM images showing fracture surfaces of the alloys tested in 3.5% NaCl in T4 condition (a), (b) 7449 (c), (d) 7449+Ag and in T76 condition (e), (f) 7449 (g), (h) 7449+Ag. (For interpretation of the references to color in this figure, the reader is referred to the web version of this article).

samples in T76 had a higher OCP relative to the T4 condition. After PDP as shown in Fig. 15 (b), a shift to higher corrosion potentials (E_{corr}) in T76 relative to T4 was equally observed and Ag was found to have no influence on the E_{corr} determined from the Tafel extrapolation. This shift of the E_{corr} to higher potentials after T76 aging indicates a decrease in susceptibility to corrosion [5,19].

The anodic region of the PDP curves in Fig. 15 (b) shows a rapid increase in the current density from E_{corr}, with no clear pitting potential, suggesting the occurrence of pitting at OCP. The corresponding current density (i_{corr}) results from the Tafel extrapolation in Table 3 indicate an increase in the corrosion rate with Ag addition, despite no change in

E_{corr}. This could be due to an increase in microgalvanic activity between the Ag-rich phase and the Al-matrix in 7449+Ag.

The IGC test results are shown in Fig. 16. The SEM BSE images in Fig. 16 (a) – (d) show that the corrosion morphology is a combination of grain boundary and pitting/adjacent matrix attack. A higher corrosion rate was observed in 7449+Ag relative to 7449 as indicated by the corrosion penetration depth and mass loss results in Fig. 16 (e). As expected, a decrease in the corrosion rate after T76 aging was observed. These were supported by the ICP-MS results in Fig. 16 (f), where a higher concentration of Al ions in the test solution was observed in 7449+Ag relative to the base alloy in both aging conditions, with the samples in
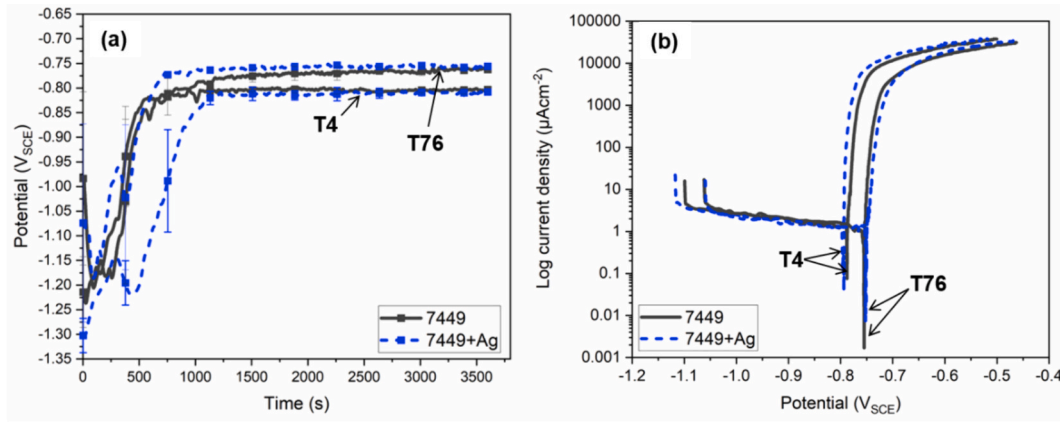
Fig. 15. OCP measurements for 1 h (a) and the corresponding PDP curves (b) in T4 and T76 conditions.

Table 3
Summary of results from PDP measurements of alloys in T4 and T76 conditions.

Alloys	OCP (V_{SCE})	E_{corr} (V_{SCE})	i_{corr} (μAcm^{-2})
7449 (T4)	− 0.803 ± 0.008	− 0.783 ± 0.012	0.993 ± 0.387
7449+Ag (T4)	− 0.808 ± 0.008	− 0.794 ± 0.003	1.627 ± 0.370
7449 (T76)	− 0.763 ± 0.004	− 0.751 ± 0.009	1.061 ± 0.273
7449+Ag (T76)	− 0.756 ± 0.004	− 0.751 ± 0.002	1.529 ± 0.626

T76 condition having lower values than in T4 condition as expected. This again confirms that 0.4 wt% Ag addition is detrimental to the corrosion resistance of 7449 alloy after 6 h of immersion in the IGC test solution, which agrees with both the SSRT and the PDP test results.

4. Discussion

4.1. Influence of Ag on microstructure, precipitation behavior and chemistry

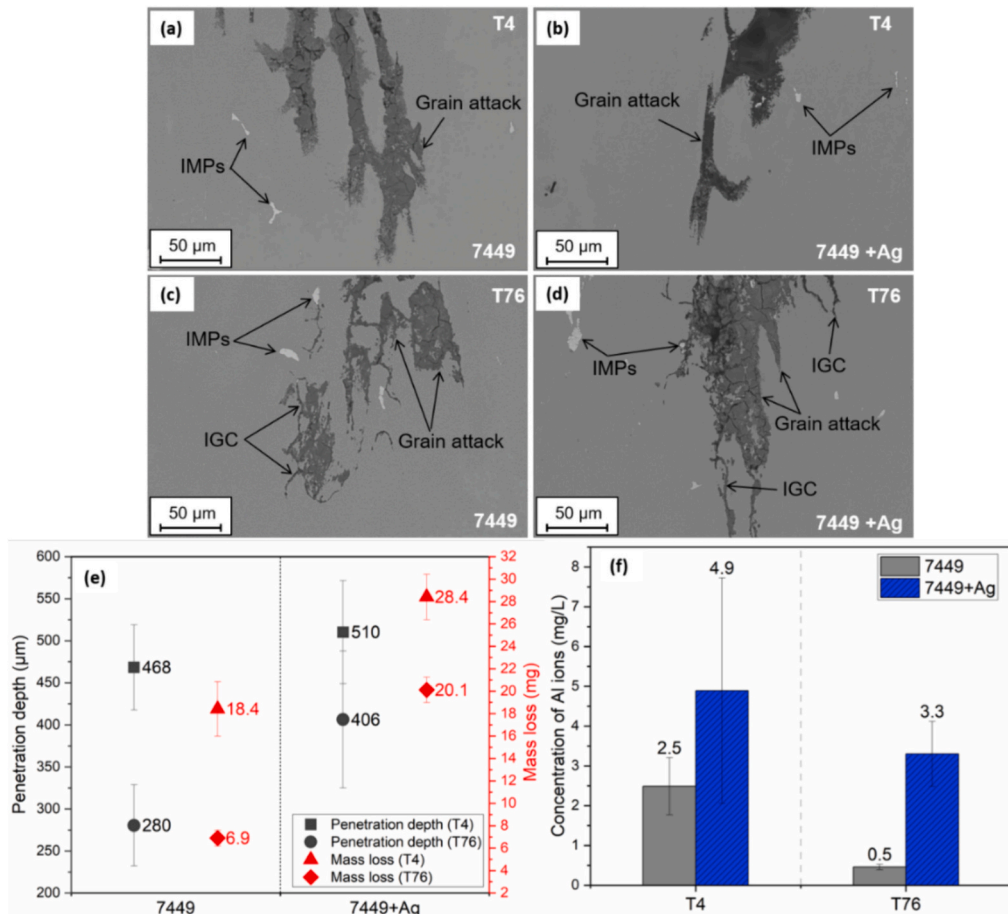Ag addition in 7xxx alloys was revisited by investigating its influence

Fig. 16. SEM BSE images showing the corrosion morphology in T4 (a) 7449 (b) 7449+Ag and in T76 (c) 7449 (d) 7449+Ag. The measured corrosion penetration depth with mass loss after test and the corresponding ICP – MS results of the Al ion concentration are shown in (e) and (f), respectively.

on grain size, eutectic phase solvus, matrix precipitates/intermetallic particles, GBP composition, PFZ width and GB segregation in 7449 alloy (Zn/Mg of 4). The incorporation of Ag atoms in the eutectic Mg(Zn,Cu, Al)$_2$ phase stabilizes it by increasing the solvus temperature, as shown by the DSC results in Fig. 4 and reported in a previous investigation on an Al-Zn-Mg-Cu-Ge-Ag alloy [68]. It is unclear when the Ag-rich AlAgZnMgCu phase, which was first observed in the T4 condition, formed in 7449+Ag. However, as earlier stated, the presence of Ag in the MPs and in the GBP in 7449+Ag suggests that some Ag atoms were in solid solution after solution heat treatment. Ag exhibits a high solid solubility limit of ~56 wt% at 566 °C (eutectic temperature) in binary Al—Ag alloys which decreases drastically to 0.4 wt% at 460 °C in an alloy containing 4 wt% Zn and 3 wt% Mg and even further down to 0.15 wt% when the Zn content is increased to 8 wt% [30]. Hence, it can be concluded that the AlAgZnMgCu phase is formed due to the high Zn content and the presence of Mg in 7449 alloy which lowered the solubility limit of Ag. After solution treatment, Ag in solid solution enhances stable cluster formation at RT or during early stages of artificial aging due to the strong attractive interaction of Ag with vacancies (Va) and solute atoms in Al [14,18]. Density functional theory (DFT) calculations in Table 4 show that the driving force for cluster formation is enhanced with Ag as indicated by the high solute-solute, solute-Va and solute-solute-Va binding energies. These stable clusters act as precursors for GP zones formation and increase the number density of the strengthening η' precipitates [18,21]. Since Ag contributes to cluster formation, the partitioning of Ag in the precipitates is therefore expected and explains the presence of Ag in the MPs and GBP (Table 2)

Although not observed in the present study, enhanced polyhedral T-type clusters are believed to form with Ag addition in Al alloys during the early stages of aging, which contributes to enhanced strengthening [18,27]. The absence of the T-Mg$_{32}$(Al,Zn,Cu)$_{49}$ phase in the studied alloys after T76 aging is not surprising since this phase mainly precipitates in alloys with a low Zn/Mg ratio or after prolonged aging [14]. Also, the measured Zn/Mg ratio of the MPs by APT shown in Table 2 are well above the Zn/Mg ratio (≈ 0.9) of the T-type phase [18]. Nevertheless, the presence of a rod-shaped η-type MPs with a high Zn content in 7449+Ag could be interpreted as precipitation from Zn-rich clusters resulting from the high Zn content of the alloy. Since PFZ formation is strongly dependent on the solute/vacancy concentration adjacent to the GBs after solution treatment [17,31], the precipitation of the Ag-rich AlAgZnMgCu phase in 7449+Ag will essentially deplete vacancies and solute atoms necessary to form stable clusters and precipitates in the matrix during the T76 aging. This could explain why no decrease in the PFZ width in 7449+Ag relative to 7449 was observed.

4.2. Ag impact on hardness and mechanical properties

Precipitation hardening in the studied 7xxx alloys entails the interaction of precipitates with dislocations, with maximum strength achieved by the particle shear mechanism described by the Kochs statistical model in Eq. 2 [70].

$$\sigma = 0.6MGb \left[\frac{2\sqrt{f_v}}{\left(d / \left(\pi/4 \right) \right)} \right] \qquad (2)$$

Where σ: Strengthening effect, M: Taylor factor, G: Shear modulus, b: Burgers vector, f_v: Precipitate volume fraction and d: Average diameter of precipitates. This strengthening mechanism is obtainable in the presence of coherent/semi-coherent precipitates of a critical size above which a change from particle shear to Orowan hardening mechanism, due to coherency loss, occurs leading to a decrease in strength [23]. The Ashby-Orowan relationship [71] in Eq. 3 describes the strengthening mechanism in the presence of non-shearable (hard) particles.

$$\sigma = \left[\frac{0.538Gbf_v^{1/2}}{d} \right] ln \left(d/2b \right) \qquad (3)$$

Where σ, G, b, f_v and d are as described above. According to Eqs. (2) and (3), a higher volume fraction of precipitates and a smaller precipitate radius (up to the critical radius) result in increased strengthening.

The interplay of particle shear and orowan hardening mechanisms can be seen in the hardness results in Fig. 12 where hardness increases during artificial aging at 121 °C from the T4 condition due to the formation and growth of fine precipitates to optimum size, and decreases slightly after moderate overaging to the T76 condition when precipitate coarsening occurs. Figs. 12 and 13 show that the addition of Ag clearly results in an increase in strength in the T4 condition which could suggest enhanced cluster formation or a natural aging response relative to the base alloy. In fact, this behavior could also be attributed to the presence of the AlAgZnMgCu phase which contributed to an increase in strength. Although this observation in the T4 condition corroborates previous findings in moderate Zn 7xxx alloys [14,18,19,21], an unforeseen slight decrease in strength after T76 aging was observed in 7449+Ag. Referring to the APT results on precipitate size and volume fraction in the T76 condition, the strength contribution by spherical MPs in 7449 and the dominant rod-shaped MPs in 7449+Ag can be calculated from Eq. (3). Using M = 2 [70], G and b for Al = 26,200 MPa and 0.286 nm [71], respectively, the results of the calculation in Table 5 indicates no significant difference in the average strength contribution by precipitates with Ag addition in 7449 after T76 aging. However, it is important to note that the total yield strength is defined by the sum of the intrinsic strength (σ$_\alpha$), GB (Hall-Petch) strengthening (σ$_{GB}$), solid solution strengthening (σ$_{SS}$) and strengthening due to precipitates (σ$_{MPs}$) as shown in Eq. (4) [70].

$$\sigma = \sigma_\alpha + \sigma_{GB} + \sigma_{SS} + \sigma_{MPs} \qquad (4)$$

Since σ$_\alpha$ is constant (10–18 MPa) [70] in both alloys, the marginal decrease in strength in 7449+Ag after T76 aging would have resulted from lower σ$_{GB}$ and σ$_{SS}$ relative to 7449, owing to the larger average grain size and the depletion of solute atoms from solid solution by the AlAgZnMgCu phase, respectively.

4.3. Stress corrosion cracking (SCC) and localized corrosion behavior with Ag addition

SCC of 7xxx alloys in NaCl solution initiates from critical defects resulting from localized corrosion after the breakdown of the protective native oxide layer which occurred under free corrosion potential in the

Table 4
DFT binding energies of solute-solute, solute-Va and solute-solute-Va clusters in Al [69].

Solute-solute cluster	Binding energy x 10^{-3} (eV)	Solute-Va cluster	Binding energy x 10^{-3} (eV)	Solute-solute-Va cluster	Binding energy x 10^{-3} (eV)
Cu – Zn	30	Mg – Va	10	Mg – Va – Zn	100
Mg – Zn	40	Zn – Va	50	Mg – Va – Cu	100
Mg – Cu	20	Cu – Va	30	Mg – Va – Ag	190
Mg – Ag	90	Ag – Va	110		
Zn – Ag	55[a]				

[a] Extracted from Ogura et al. [17].

Table 5
Estimation and comparison of strength contribution of precipitates with Ag addition in 7449.

Alloy	d of MPs (nm)	f_v of MPs (%)	σ$_{MPs}$ (MPa)
7449	6 ± 3	5.9	408 ± 99
7449+Ag	5 ± 1	5.4	409 ± 36

studied alloys as shown by the PDP results in Fig. 15 (b). These defects form in the vicinity of cathodic IMPs (Al$_7$Cu$_2$Fe or Mg$_2$Si after selective Mg dissolution) as pits in the matrix or as fissures at the GBs due to an electrochemical potential gradient [63]. Localized corrosion near the IMPs and at the GBs was observed in the fractography images in Fig. 14 and the IGC cross section images in Fig. 16, respectively. Furthermore, going by the high Ag content of the AlAgZnMgCu phase in 7449+Ag, it is presumably strongly cathodic and could have directly resulted in accelerated localized corrosion and increased critical surface defects, as indicated by the higher current density and IGC rate in Table 3 and Fig. 16, respectively. However, the verification of the evidence of localized corrosion at the nano-size AlAgZnMgCu phase was not possible at the resolution of the SEM and remains to be investigated. During SSRT in NaCl solution, a rapid change in the electrolyte conditions inside these flaws occurs due to metal cation (Al^{3+}) hydrolysis leading to local acidification and the subsequent atomic hydrogen production by cathodic reaction as shown in Eqs. (5)–(7) below [7,61,63].

$$Al \rightarrow Al^{3+} + 3e^- \tag{5}$$

$$Al^{3+} + 3H_2O \rightarrow Al(OH)_3 + 3H^+ \tag{6}$$

$$H^+ + e^- \rightarrow H \tag{7}$$

The hydrogen can diffuse into the lattice or readily along the GBs and lead to embrittlement and SCC propagation from the critical defects (prone to high stress concentrations) which can occur in synergy with anodic dissolution of the GB precipitates [48,62]. The GB microstructure, particularly the composition of the η-Mg(Zn,Cu,Al)$_2$ phase, controls the anodic dissolution rate which also affects the rate of cathodic hydrogen generation [7]. In 7449+Ag, Ag partitioning of up to 1–3 at. % in the GB η-Mg(Zn,Cu,Al)$_2$ phase was observed. However, it is unclear to what extent this increases the nobility of the GB η-Mg(Zn,Cu,Al)$_2$ phase in 7449+Ag, since the alloy showed a higher SCC and IGC susceptibility after stable precipitation in T76 condition due to the presence of the AlAgZnMgCu phase.

On the influence of aging condition, the grain boundaries are sparsely populated by the small quench-induced η-Mg(Zn,Cu,Al)$_2$ phase in the T4 condition relative to the GBPs in the T76 condition as shown by the STEM images in Fig. 8. This means that in the T4 condition, anodic dissolution of the η-Mg(Zn,Cu,Al)$_2$ phase is less favorable and hydrogen migration and embrittlement along the GBs can occur easily. In addition, equilibrium and non-equilibrium segregation of Zn and Mg by solute partitioning or vacancy drag effect occurs at the GBs during quenching from solution heat treatment. Mg segregation levels of up to 4.5 at.% has been measured in the as-quenched condition of an Al-6.2Zn-2.5Mg-2.1Cu alloy [56], which is much higher than the segregation level after artificial aging, as indicated by the APT results in Table 2. Mg at the GBs has been reported to promote hydrogen uptake, transport and HEDE [7,65,72,73], which will occur readily in the T4 condition relative to the T76 condition due to solute supersaturation during quenching. Therefore, in the T4 condition (Fig. 14 (b) and (d)), hydrogen at the GBs weakens the interatomic bonds (at the critical concentration) leading to tensile detachment of atoms and resulting in IGSCC by the HEDE mechanism [62,73].

The observed regions of TGSCC near the sample edges in the T4 condition would have initiated from pits in the matrix, followed by atomic hydrogen at the crack tip weakening the cohesive force (HEDE) or facilitating dislocation movement and subsequent crack propagation by the HELP and/or the AIDE mechanisms [62]. In the AIDE mechanism proposed by Lynch [67], adsorbed hydrogen at the crack tip weakens the interatomic bonds, thereby facilitating dislocation movement on slip planes and micro- or nano-void formation at the interface of second phase particles ahead of the crack tip. This results in transgranular crack propagation by alternate slip and void coalescence. These voids can form at the interface of the small quench-induced η-Mg(Zn,Cu,Al)$_2$ phase

in the T4 condition by the HELP or HEDE mechanism, indicating that these mechanisms often occur in synergy. Recent investigations [74,75] supported by DFT calculations have shown that preferential hydrogen trapping in high-Zn Al-10Zn-1Mg alloys occurs at the η–MgZn$_2$/Al-matrix interface rather than at GBs or dislocations, resulting in the deterioration of the cohesive force of the interface when the critical hydrogen concentration is reached, and leading to quasi-cleavage fracture. Since IGSCC was largely not observed in the T76 condition, it can be concluded that the rate of hydrogen entry and transport during SSRT in 3.5% NaCl solution is higher than the anodic dissolution rate of the GBPs. Therefore, the dominance of TGSCC after T76 aging could be explained by the enhanced hydrogen trapping at the interface of the η-Mg(Zn,Cu,Al)$_2$ phase and the presence of less sensitive GBs due to decreased Mg segregation level owing to precipitation [65,72]. The increased sensitivity in 7449+Ag in T76 condition will therefore result from enhanced hydrogen production at the cathodic AlAgZnMgCu phase, which can diffuse ahead of a crack tip and get trapped at the η/matrix interface, thus decreasing the time required to reach the critical hydrogen concentration necessary to cause embrittlement.

Hence, in order to further explore the potentials of minor Ag addition in current or future high-strength 7xxx alloy developments, alloy chemistry modification with Ag should be carried out at concentrations below the solubility limit, which is believed to be strongly dependent on the Zn content. This will suppress the formation of the Ag-rich AlAgZnMgCu phase. Whether this will result in improved mechanical and aqueous corrosion properties in a high-Zn 7xxx alloy remains to be investigated.

5. Conclusion

The influence of 0.4 wt% Ag addition on the microstructure, mechanical properties, stress corrosion cracking and localized corrosion behavior of a 7xxx alloy with Zn/Mg ratio $\approx$ 4 was investigated using a range of complementary characterization techniques and established mechanical and corrosion testing methods. The following can be concluded.

1. Ag dissolves in the eutectic η-Mg(Zn,Cu,Al)$_2$ phase and increases the solvus temperature of the phase in the as-cast condition. After solution treatment, Ag is partially in solid solution with the excess forming nano-sized Ag-rich AlAgZnMgCu phase due to a decrease in its solubility limit at high Zn content. This phase is presumably cathodic with the Al matrix going by its high Ag content.

2. Ag partitioning in the matrix precipitates (MPs) and grain boundary precipitates (GBPs) occurs with Ag addition in 7449. In the T4 condition, nano-sized quench-induced η-Mg(Zn,Cu,Al)$_2$ precipitates form at the GBs, in the base alloy and in the Ag-modified alloy. The Mg, Zn and Cu contents of the quench-induced η-Mg(Zn,Cu,Al)$_2$ remain similar in both alloys and Ag of about 3 at. % dissolves in the phase. After T76 aging, the MPs and GBPs in the Ag-modified alloy dissolve only about 1 at. % Ag. No decrease in the PFZ width occurs with Ag addition in 7449 alloy after T76 aging.

3. Although an increase in hardness and tensile properties occurs with minor Ag addition in the T4 condition, enhanced age hardening response and precipitation kinetics during artificial aging at 121 °C do not occur. No difference in strength contribution by precipitates occurs with 0.4 wt% Ag addition in 7449 after T76 aging.

4. Ag addition in the high-Zn 7449 alloy is detrimental to SCC under continuous loading and localized corrosion in the T4 and T76 conditions. Regardless of the Ag partitioning in the GBPs in the Ag-modified alloy, SCC, pitting and IGC susceptibility increase relative to the base alloy. This is mainly due to enhanced corrosion resulting from the increased electrochemical potential gradient at the cathodic AlAgZnMgCu phase.

CRediT authorship contribution statement

Chijioke Kenneth Akuata: Writing – review & editing, Writing – original draft, Methodology, Investigation, Formal analysis, Data curation, Conceptualization. **Lisa T. Belkacemi:** Writing – review & editing, Investigation. **Daniela Zander:** Writing – review & editing, Supervision, Project administration, Funding acquisition, Conceptualization.

Declaration of competing interest

The authors declare that they have no known competing financial interests or personal relationships that could have appeared to influence the work reported in this paper.

Data availability

The raw/processed data required to reproduce these findings cannot be shared at this time as the data also forms part of an ongoing study.

Acknowledgement

References

[1] T. Dursun, C. Soutis, Recent developments in advanced aircraft aluminium alloys, Mater. Des. 56 (2014) (1980-2015) 862–871, https://doi.org/10.1016/j.matdes.2013.12.002.

[2] B. Zhou, B. Liu, S. Zhang, The advancement of 7XXX series aluminum alloys for aircraft structures. A review, Metals 11 (5) (2021), https://doi.org/10.3390/met11050718.

[3] P.A. Rometsch, Y. Zhang, S. Knight, Heat treatment of 7xxx series aluminium alloys—some recent developments, Trans. Nonferrous Metals Soc. China 24 (7) (2014) 2003–2017, https://doi.org/10.1016/S1003-6326(14)63306-9.

[4] A. Heinz, A. Haszler, C. Keidel, S. Moldenhauer, R. Benedictus, W.S. Miller, Recent development in aluminium alloys for aerospace applications, Mater. Sci. Eng. A 280 (1) (2000) 102–107, https://doi.org/10.1016/S0921-5093(99)00674-7.

[5] C.K. Akuata, F.R. Gunawan, P. Suwanpinij, D. Zander, Microstructure evolution and localized corrosion susceptibility of an Al-Zn-Mg-Cu-Zr 7xxx alloy with minor Cr addition, Materials 16 (3) (2023), https://doi.org/10.3390/ma16030946.

[6] N.J.H. Holroyd, T.L. Burnett, J.J. Lewandowski, G.M. Scamans, Environment-induced cracking of high-strength Al-Zn-Mg-Cu aluminum alloys: past, Present Fut. Corros. 79 (1) (2022) 48–71, https://doi.org/10.5006/4149.

[7] N.J.H. Holroyd, Environmentally-Induced Cracking of High-Strength Aluminum Alloys, Environmentally-Induced Cracking of Metals, National Association of Corrosion Engineers, 1989, pp. 311–345.

[8] H. Holroyd, T. Burnett, G. Scamans, Environment-induced crack initiation and early stages of crack growth in aluminum alloys, Corrosion 79 (1) (2023) 3, https://doi.org/10.5006/4275.

[9] U. De Francisco, N.O. Larrosa, M.J. Peel, Hydrogen environmentally assisted cracking during static loading of AA7075 and AA7449, Mater. Sci. Eng. A 772 (2020) 138662, https://doi.org/10.1016/j.msea.2019.138662.

[10] E. Schwarzenböck, E. Ollivier, A. Garner, A. Cassell, T. Hack, Z. Barrett, C. Engel, T. L. Burnett, N.J.H. Holroyd, J.D. Robson, P.B. Prangnell, Environmental cracking performance of new generation thick plate 7000-T7x series alloys in humid air, Corros. Sci. 171 (2020) 108701, https://doi.org/10.1016/j.corsci.2020.108701.

[11] J.T. Staley, 1 - History of wrought-aluminum-alloy development, in: A. K. Vasudevan, R.D. Doherty (Eds.), Treatise on Materials Science & Technology, Elsevier, 1989, pp. 3–31.

[12] I.J. Polmear, A trace element effect in alloys based on the aluminium-zinc-magnesium system, Nature 186 (4721) (1960) 303–304, https://doi.org/10.1038/186303a0.

[13] Y. Baba, Influence of addition of Ag or Cu on the formation of G.P. zone in Al-Zn alloy, J. Jpn. Inst. Metals 30 (7) (1966) 679–683, https://doi.org/10.2320/jinstmet1952.30.7_679.

[14] I.J. Polmear, The influence of small additions of silver on the structure and properties of aged aluminum alloys, JOM 20 (6) (1968) 44–51, https://doi.org/10.1007/BF03378722.

[15] J.T. Staley, R.H. Brown, R. Schmidt, Heat treating characteristics of high strength Al-Zn-Mg-Cu alloys with and without silver additions, Metall. Mater. Trans. B Process Metall. Mater. Process. Sci. 3 (1) (1972) 191–199, https://doi.org/10.1007/BF02680598.

[16] T. Ogura, S. Hirosawa, T. Sato, Quantitative characterization of precipitate free zones in Al–Zn–Mg alloys by microchemical analysis and nanoindentation measurement, Sci. Technol. Adv. Mater. 5 (4) (2004) 491–496, https://doi.org/10.1016/j.stam.2004.02.007.

[17] T. Ogura, S. Hirosawa, A. Cerezo, T. Sato, Atom probe tomography of nanoscale microstructures within precipitate free zones in Al–Zn–Mg(–Ag) alloys, Acta Mater. 58 (17) (2010) 5714–5723, https://doi.org/10.1016/j.actamat.2010.06.046.

[18] Y. Wang, X. Wu, L. Cao, X. Tong, Y. Zou, Q. Zhu, S. Tang, H. Song, M. Guo, Effect of Ag on aging precipitation behavior and mechanical properties of aluminum alloy 7075, Mater. Sci. Eng. A 804 (2021) 140515, https://doi.org/10.1016/j.msea.2020.140515.

[19] S. Wang, C. He, B. Luo, Z. Bai, G. Jiang, The role of trace Ag in controlling the precipitation and stress corrosion properties of aluminium alloy 7N01, Vacuum 184 (2021) 109948, https://doi.org/10.1016/j.vacuum.2020.109948.

[20] S.K. Caraher, I.J. Polmear, S.P. Ringer, Effects of Cu and Ag on precipitation in Al-4Zn-3Mg(wt.%), in: International Conference on Aluminium Alloys (ICAA), Tokyo, Japan, 1998, pp. 739–744.

[21] S.K. Maloney, K. Hono, I.J. Polmear, S.P. Ringer, The effects of a trace addition of silver upon elevated temperature ageing of an Al–Zn–Mg alloy, Micron 32 (8) (2001) 741–747, https://doi.org/10.1016/S0968-4328(00)00081-0.

[22] R. Ferragut, A. Dupasquier, M.M. Iglesias, C.E. Macchi, A. Somoza, I.J. Polmear, Vacancy-solute aggregates in Al-Zn-Mg-(Cu, Ag), Mater. Sci. Forum 519-521 (2006) 309–314, https://doi.org/10.4028/www.scientific.net/MSF.519-521.309.

[23] C.K. Akuata, C. Altenbach, C. Schnatterer, P. Suwanpinij, C. Saiyasombat, D. Zander, Age hardening response of AA7108A investigated by means of synchrotron-based X-ray absorption spectroscopy (XAS) measurements, Mater. Sci. Eng. A 747 (2019) 42–52, https://doi.org/10.1016/j.msea.2019.01.052.

[24] L.K. Berg, J. Gjønnes, V. Hansen, X.Z. Li, M. Knutson-Wedel, G. Waterloo, D. Schryvers, L.R. Wallenberg, GP-zones in Al–Zn–Mg alloys and their role in artificial aging, Acta Mater. 49 (17) (2001) 3443–3451, https://doi.org/10.1016/S1359-6454(01)00251-8.

[25] V. Hansen, O.B. Karlsen, Y. Langsrud, J. Gjønnes, Precipitates, zones and transitions during aging of Al-Zn-Mg-Zr 7000 series alloy, Mater. Sci. Technol. 20 (2) (2004) 185–193, https://doi.org/10.1179/026708304225010424.

[26] X.B. Yang, J.H. Chen, J.Z. Liu, F. Qin, J. Xie, C.L. Wu, A high-strength AlZnMg alloy hardened by the T-phase precipitates, J. Alloys Compd. 610 (2014) 69–73, https://doi.org/10.1016/j.jallcom.2014.04.185.

[27] J.H. Auld, J.T. Vietz, I.J. Polmear, T-phase precipitation induced by the addition of silver to an Aluminium–copper–magnesium alloy, Nature 209 (5024) (1966) 703–704, https://doi.org/10.1038/209703a0.

[28] H.Y. Hunsicker, J.T. Staley, R.H. Brown, Stress-corrosion resistance of high-strength Al-Zn-Mg-Cu alloys with and without silver additions, Metall. Mater. Trans. B 3 (1) (1972) 201–209, https://doi.org/10.1007/BF02680599.

[29] X.Z. Wu, D.H. Xiao, Z.M. Zhu, X.X. Li, K.H. Chen, Effect of minor silver addition on microstructure and properties of Al-8Zn-1.Cu-1.3Mg-0.1Zr alloys, Adv. Mater. Res. 834-836 (2014) 360–363, https://doi.org/10.4028/www.scientific.net/AMR.834-836.360.

[30] L.F. Mondolfo, Structure of the aluminium: magnesium: zinc alloys, Metall. Rev. 16 (1) (1971) 95–124, https://doi.org/10.1179/mtlr.1971.16.1.95.

[31] S. Hirosawa, Y. Oguri, T. Ogura, T. Sato, Formation mechanisms of precipitate free zones in age-hardenable Al alloys, in: 9th International Conference on Aluminium Alloys, Brisbane, Australia, Institute of Materials Engineering Australasia Ltd, 2004, pp. 666–671.

[32] A.K. Mukhopadhyay, K.S. Prasad, V. Kumar, G.M. Reddy, S.V. Kamat, V.K. Varma, Key microstructural features responsible for improved stress corrosion cracking resistance and weldability in 7xxx series Al alloys containing Micro / trace alloying additions, Mater. Sci. Forum 519-521 (2006) 315–320, https://doi.org/10.4028/www.scientific.net/MSF.519-521.315.

[33] T. Ogura, A. Hirose, T. Sato, Effect of PFZ and grain boundary precipitate on mechanical properties and fracture morphologies in Al-Zn-Mg(Ag) alloys, Mater. Sci. Forum 638-642 (2010) 297–302, https://doi.org/10.4028/www.scientific.net/MSF.638-642.297.

[34] L. Lin, Z. Liu, W. Liu, Y. Zhou, T. Huang, Effects of ag addition on precipitation and fatigue crack propagation behavior of a medium-strength Al–Zn–Mg alloy, J. Mater. Sci. Technol. 34 (3) (2018) 534–540, https://doi.org/10.1016/j.jmst.2016.11.008.

[35] A.K. Mukhopadhyay, Microstructure and properties of high strength aluminium alloys for structural applications, Trans. Indian Inst. Metals 62 (2) (2009) 113–122, https://doi.org/10.1007/s12666-009-0015-z.

[36] G. Cliff, G.W. Lorimer, The quantitative analysis of thin specimens, J. Microsc. 103 (2) (1975) 203–207, https://doi.org/10.1111/j.1365-2818.1975.tb03895.x.

[37] A. Garner, R. Euesden, Y. Yao, Y. Aboura, H. Zhao, J. Donoghue, M. Curioni, B. Gault, P. Shanthraj, Z. Barrett, C. Engel, T.L. Burnett, P.B. Prangnell, Multiscale analysis of grain boundary microstructure in high strength 7xxx Al alloys, Acta Mater. 202 (2021) 190–210, https://doi.org/10.1016/j.actamat.2020.10.021.

[38] B. Geiser, D. Larson, E. Oltman, S. Gerstl, D. Reinhard, T. Kelly, T. Prosa, Wide-field-of-view atom probe reconstruction, Microsc. Microanal. 15 (S2) (2009) 292–293, https://doi.org/10.1017/s1431927609098249.

[39] ASTM, ASTM G129–21:Standard Practice for Slow Strain Rate Testing to Evaluate the Susceptibility of Metallic Materials to Environmentally Assisted Cracking, ASTM International, Pennsylvania, USA, 2021.

[40] ASTM, ASTM, G110 : Standard Practice for Evaluating Intergranular Corrosion Resistance of Heat Treatable Aluminum Alloys by Immersion in Sodium Chloride + Hydrogen Peroxide Solution, ASTM International, Pennsylvania, USA, 2003.

[41] H. Zhang, D. Yang, X. Chen, H. Nagaumi, Z. Wu, C. Guo, J. Zou, P. Wang, K. Qin, J. Cui, Influence of ag on microstructure, mechanical properties and tribological properties of as-cast Al-33Zn-2Cu high-zinc aluminum alloy, J. Alloys Compd. 922 (2022) 166157, https://doi.org/10.1016/j.jallcom.2022.166157.

[42] A. Ghosh, M. Ghosh, R. Kalsar, Influence of homogenisation time on evolution of eutectic phases, dispersoid behaviour and crystallographic texture for Al–Zn–Mg–Cu–Ag alloy, J. Alloys Compd. 802 (2019) 276–289, https://doi.org/10.1016/j.jallcom.2019.06.091.

[43] D.E. Newbury, Mistakes encountered during automatic peak identification of minor and trace constituents in electron-excited energy dispersive X-ray microanalysis, Scanning 31 (3) (2009) 91–101, https://doi.org/10.1002/sca.20151.

[44] W. Wang, R.T. Shuey, Homogenization Model for 7xxx Aluminum Alloys, 12th International Conference on Aluminium Alloys, The Japan Institute of Light Metals, Yokohama, Japan, 2010, pp. 264–269.

[45] R. Huang, M. Li, H. Yang, S. Lu, H. Zuo, S. Zheng, Y. Duan, X. Yuan, Effects of Mg contents on microstructures and second phases of as-cast Al–Zn–Mg–Cu alloys, J. Mater. Res. Technol. 21 (2022) 2105–2117, https://doi.org/10.1016/j.jmrt.2022.10.050.

[46] A.K. Mukhopadhyay, Q.B. Yang, S.R. Singh, The influence of zirconium on the early stages of aging of a ternary Al Zn Mg alloy, Acta Metall. Mater. 42 (9) (1994) 3083–3091, https://doi.org/10.1016/0956-7151(94)90406-5.

[47] X.J. Jiang, J. Tafto, B. Noble, B. Holme, G. Waterloo, Differential scanning calorimetry and electron diffraction investigation on low-temperature aging in Al-Zn-Mg alloys, Metall. Mater. Trans. A 31 (2) (2000) 339–348, https://doi.org/10.1007/s11661-000-0269-x.

[48] C. Altenbach, C. Schnatterer, U.A. Mercado, J.-P. Suuronen, D. Zander, G. Requena, Synchrotron-based holotomography and X-ray fluorescence study on the stress corrosion cracking behavior of the peak-aged 7075 aluminum alloy, J. Alloys Compd. 817 (2020) 152722, https://doi.org/10.1016/j.jallcom.2019.152722.

[49] X. Peng, Q. Guo, X. Liang, Y. Deng, Y. Gu, G. Xu, Z. Yin, Mechanical properties, corrosion behavior and microstructures of a non-isothermal ageing treated Al-Zn-Mg-Cu alloy, Mater. Sci. Eng. A 688 (2017) 146–154, https://doi.org/10.1016/j.msea.2017.01.086.

[50] H. Löffler, I. Kovács, J. Lendvai, Decomposition processes in Al-Zn-Mg alloys, J. Mater. Sci. 18 (8) (1983) 2215–2240, https://doi.org/10.1007/BF00541825.

[51] D.J. Lloyd, M.C. Chaturvedi, A calorimetric study of aluminium alloy AA-7075, J. Mater. Sci. 17 (6) (1982) 1819–1824, https://doi.org/10.1007/BF00540811.

[52] X.Z. Li, V. Hansen, J. GjØnnes, L.R. Wallenberg, HREM study and structure modeling of the η' phase, the hardening precipitates in commercial Al–Zn–Mg alloys, Acta Mater. 47 (9) (1999) 2651–2659, https://doi.org/10.1016/S1359-6454(99)00138-X.

[53] A. Deschamps, Y. Bréchet, Influence of quench and heating rates on the ageing response of an Al–Zn–Mg–(Zr) alloy, Mater. Sci. Eng. A 251 (1) (1998) 200–207, https://doi.org/10.1016/S0921-5093(98)00615-7.

[54] K. Stiller, P.J. Warren, V. Hansen, J. Angenete, J. Gjønnes, Investigation of precipitation in an Al–Zn–Mg alloy after two-step ageing treatment at 100° and 150°C, Mater. Sci. Eng. A 270 (1) (1999) 55–63, https://doi.org/10.1016/S0921-5093(99)00231-2.

[55] J.X. Zang, K. Zhang, S.I. Dai, Precipitation behavior and properties of a new high strength Al-Zn-Mg-Cu alloy, Trans. Nonferrous Metals Soc. China 22 (11) (2012) 2638–2644, https://doi.org/10.1016/S1003-6326(11)61511-2.

[56] H. Zhao, Segregation and Precipitation at Interfaces in a Model Al-Zn-Mg-Cu Alloy, Dissertation, Rheinisch-Westfälische Technische Hochschule Aachen, 2019.

[57] M. Dumont, W. Lefebvre, B. Doisneau-Cottignies, A. Deschamps, Characterisation of the composition and volume fraction of η' and η precipitates in an Al–Zn–Mg

[58] J. Gjønnes, C.J. Simensen, An electron microscope investigation of the microstructure in an aluminium-zinc-magnesium alloy, Acta Metall. 18 (8) (1970) 881–890, https://doi.org/10.1016/0001-6160(70)90076-7.

[59] G. Sha, A. Cerezo, Early-stage precipitation in Al–Zn–Mg–Cu alloy (7050), Acta Mater. 52 (15) (2004) 4503–4516, https://doi.org/10.1016/j.actamat.2004.06.025.

[60] G.M. Scamans, R. Alani, P.R. Swann, Pre-exposure embrittlement and stress corrosion failure in Al Zn mg alloys, Corros. Sci. 16 (7) (1976) 443–459, https://doi.org/10.1016/0010-938X(76)90065-2.

[61] M.O. Speidel, Stress corrosion cracking of aluminum alloys, Metall. Trans. A. 6 (1975) 631–651, https://doi.org/10.1007/BF02672284.

[62] T.D. Burleigh, The postulated mechanisms for stress corrosion cracking of aluminum alloys: a review of the literature 1980-1989, Corrosion 47 (2) (1991) 89–98, https://doi.org/10.5006/1.3585235.

[63] D. Najjar, T. Magnin, T.J. Warner, Influence of critical surface defects and localized competition between anodic dissolution and hydrogen effects during stress corrosion cracking of a 7050 aluminium alloy, Mater. Sci. Eng. A 238 (2) (1997) 293–302, https://doi.org/10.1016/S0921-5093(97)00369-9.

[64] R. Braun, Environmentally Assisted Cracking of Aluminium Alloys in Chloride Solutions, ICAA, The Japan Institute of Light Metals, Toyohashi, Japan, 1998, pp. 153–163.

[65] R.G. Song, W. Dietzel, B.J. Zhang, W.J. Liu, M.K. Tseng, A. Atrens, Stress corrosion cracking and hydrogen embrittlement of an Al–Zn–Mg–Cu alloy, Acta Mater. 52 (16) (2004) 4727–4743, https://doi.org/10.1016/j.actamat.2004.06.023.

[66] R. Gest, A. Troiano, Stress corrosion and hydrogen embrittlement in an aluminum alloy, Corrosion 30 (8) (1974) 274–279.

[67] S.P. Lynch, 2 - hydrogen embrittlement (HE) phenomena and mechanisms, in: V. S. Raja, T. Shoji (Eds.), Stress Corrosion Cracking, Woodhead Publishing, 2011, pp. 90–130.

[68] L. Lin, Z. Liu, S. Bai, Y. Zhou, W. Liu, Q. Lv, Effects of Ge and Ag additions on quench sensitivity and mechanical properties of an Al–Zn–Mg–Cu alloy, Mater. Sci. Eng. A 682 (2017) 640–647, https://doi.org/10.1016/j.msea.2016.11.092.

[69] J. Peng, S. Bahl, A. Shyam, J.A. Haynes, D. Shin, Solute-vacancy clustering in aluminum, Acta Mater. 196 (2020) 747–758, https://doi.org/10.1016/j.actamat.2020.06.062.

[70] R. Ghiaasiaan, S. Shankar, Structure-property models in Al-Zn-Mg-Cu alloys: a critical experimental assessment of shape castings, Mater. Sci. Eng. A 733 (2018) 235–245, https://doi.org/10.1016/j.msea.2018.07.048.

[71] T. Gladman, Precipitation hardening in metals, Mater. Sci. Technol. 15 (1) (1999) 30–36, https://doi.org/10.1179/026708399773002782.

[72] G.M. Scamans, N.J.H. Holroyd, C.D.S. Tuck, The role of magnesium segregation in the intergranular stress corrosion cracking of aluminium alloys, Corros. Sci. 27 (4) (1987) 329–347, https://doi.org/10.1016/0010-938X(87)90076-X.

[73] H. Zhao, P. Chakraborty, D. Ponge, T. Hickel, B. Sun, C.-H. Wu, B. Gault, D. Raabe, Hydrogen trapping and embrittlement in high-strength Al alloys, Nature 602 (7897) (2022) 437–441, https://doi.org/10.1038/s41586-021-04343-z.

[74] T. Tsuru, K. Shimizu, M. Yamaguchi, M. Itakura, K. Ebihara, A. Bendo, K. Matsuda, H. Toda, Hydrogen-accelerated spontaneous microcracking in high-strength aluminium alloys, Sci. Rep. 10 (1) (2020) 1998, https://doi.org/10.1038/s41598-020-58834-6.

[75] Y. Xu, H. Toda, K. Shimizu, Y. Wang, B. Gault, W. Li, K. Hirayama, H. Fujihara, X. Jin, A. Takeuchi, M. Uesugi, Suppressed hydrogen embrittlement of high-strength Al alloys by Mn-rich intermetallic compound particles, Acta Mater. 236 (2022) 118110, https://doi.org/10.1016/j.actamat.2022.118110.